



Architecture, Growth Dynamics and Biomineralization of Pulsed Sr-Labelled *Katelsia rhytiphora* (Mollusca, Bivalvia)

Laura M. Otter¹, Oluwatoosin B. A. Agbaje¹, Matt R. Kilburn², Christoph Lenz^{3,4}, Hadrien Henry^{1,3}, Patrick Trimby⁵, Peter Hoppe⁶, Dorrit E. Jacob^{1,3}

5 ¹Department of Earth & Planetary Science, Macquarie University, Sydney, NSW 2109, Australia

²Centre for Microscopy Characterisation and Analysis, University of Western Australia, Perth, WA 6009, Australia

³Australian Research Council Centre of Excellence for Core to Crust Fluid System (CCFS) / GEMOC

⁴Institute of Mineralogy and Crystallography, University of Vienna, Althanstr. 14, 1090 Vienna, Austria

⁵Oxford Instruments NanoAnalysis, High Wycombe, HP12 3SE, United Kingdom

10 ⁶Particle Chemistry Department, Max Planck Institute for Chemistry, Hahn-Meitner-Weg 1, 55128 Mainz, Germany

Correspondence to: Laura M. Otter (laura.otter@mq.edu.au)

Abstract. We use pulsed Sr-labelling experiments to visualize growth of aragonitic *Katelsia rhytiphora* (Mollusca, Bivalvia) shells. The outer compound composite prismatic structure is organized into three orders of prisms, and the inner crossed acicular structure consists of intersecting lamellae. Electron Backscatter Diffraction (EBSD) reveals substantial twinning of the aragonite crystals (>46%) and an overall reduced and strategically oriented anisotropy of the Young's modulus in the whole shell compared to that of monolithic aragonite. All structural orders in both layers are enveloped by an organic sheath and the smallest mineralized units are nanogranules. Total organic contents are 2.2 (outer) and 1.4 wt.% (inner layer) and are, thus, intermediate between those of nacreous and crossed-lamellar shells. Prisms in the outer structure can be correlated to yearly, daily and sub-daily growth rates. Average daily growth rates at the ventral margin for the outer structure are 17 % higher than for the inner crossed acicular structure. The calcification front runs evenly across all structures and architectural orders independently of the current growth rate. Sharply defined transitions from labelled to unlabelled areas in the shell indicate that physiological processes driving calcification have no lag. This suggests that the extrapallial fluid cannot be very voluminous. Narrow increments of varying Sr content within labelled shell, despite constant Sr concentrations in seawater, suggest cyclic metabolic activity during calcification. Micro-Raman spectroscopy maps validate a low impact of high Sr-conditions on the aragonite crystal structure. Identical Sr-enrichment factors for labelled and ambient conditions support models of ion transport via a passive selective pathway to the mantle epithelium followed by calcification via amorphous calcium carbonate.

1 Introduction

1.1 Background

30 The shells of bivalves consist of a bio-composite material with a complex, hierarchical 3D arrangement of crystalline calcium carbonate (aragonite or calcite), intimately conjoined by organic macromolecules (Weiner and Traub, 1980; Rodriguez-



Navarro et al., 2012). This arrangement significantly enhances the physical and mechanical properties of the shell and explains its high mechanical strength (Kamat et al., 2000) and fracture resistance (Currey and Kohn, 1976; Jackson et al., 1988).

Trace elements incorporated in the carbonate phase of recent and fossil shells are used to monitor and reconstruct (paleo)environmental parameters, e.g. water salinity, temperature and pH (Jones and Quitmyer, 1996; Weiner and Dove, 2003; Gilbert et al., 2017). Although the mechanisms of mollusc shell growth, and particularly the trace element uptake mechanisms, are not yet fully understood, it is known that organic macromolecules, including polysaccharides and acidic proteins (e.g. Falini et al., 1996), control nucleation and growth of the mineral entity across all length scales (Weiner et al., 1984; Simkiss, 1965; Addadi et al., 2006; Cusack et al., 2008). Recent studies showed that the uptake of some trace elements, such as strontium, are strongly influenced by crystal growth rates, shell curvature and ontogeny in addition to physiological effects (Urey et al., 1951; Gillikin et al., 2005; Carré et al., 2005; Gillikin et al., 2008; Foster et al., 2009). Hence, a better understanding of the spatial-temporal growth dynamics of shell ultrastructures is an essential prerequisite to constrain the ability and the limitations of shells to record environmental information.

Traditionally, studies on shell formation have been focusing on the nacreous structure (Checa et al., 2006; Nudelman, 2015), but more recently, the crossed-lamellar ultrastructure, which is the most common mollusc shell structure, received increasing attention (Böhm et al., 2016; Almagro et al., 2016; Agbaje et al., 2017b). Apart from the nacreous and crossed-lamellar ultrastructure most other shell architectures have received only little attention thus far. Two of these barely investigated ultrastructures are the compound composite prismatic and crossed acicular ultrastructure, which are found in many bivalves of the Veneridae family (Shimamoto, 1986). Within this family, species of the genus *Katelsysia* are widely used for studies of hatchery production and aquaculture (Nell et al., 1994), environmental parameters (Peterson et al., 1994; Nell and Paterson, 1997; Paterson and Nell, 1997) as well as shell middens (Cann et al., 1991). *Katelsysia* shells display an outer layer with compound composite prismatic and inner layer with homogeneous (crossed acicular) structure, i.e. *venerid* shell microstructure type II (Tapetinae group Shimamoto, 1986).

Pulsed strontium labelling experiments offer an ideal way to study architectural arrangements and growth dynamics and have contributed largely to our understanding of other marine calcifiers such as scleractinian corals, echinoderms and foraminifera (Shirai et al., 2012; Nehrke et al., 2013; Domart-Coulon et al., 2014; Gorzelak et al., 2014; Gutner-Hoch et al., 2016). In this study, we firstly apply pulsed strontium labelling experiments to visualize growth dynamics in bivalve shells. The use of pulse chase labels creates “snapshots” of newly formed shell material that are later visualized and investigated by high-resolution micro- and nano-analytical methods to study the crystalline fine-structure and growth dynamics.

1.2 Compound Composite Prismatic and Crossed Acicular Ultrastructures in Mollusc Shells

The composite prismatic ultrastructure is considered one of the most complex hierarchical structures (Taylor, 1969; Popov, 1986; Shimamoto, 1986) and is an umbrella term for a family of differently arranged hierarchical prismatic structures (e.g. Popov, 1986). It consists of two prismatic orders: first-order prisms have thicknesses between 10-30 μm and run parallel to the outer shell surface, with the long axis of the prisms oriented between umbo and ventral margin of the shell (Popov, 1986).



These first-order units consist of second-order prisms with thicknesses of 0.3 μm (Shimamoto, 1986). The latter protrude radially from the centre axis of first-order prisms creating a feather-like appearance when viewed in cross-section (Taylor, 1969; Shimamoto, 1986). Each prism in both hierarchical orders is covered in a thin organic envelope (Taylor, 1969; Shimamoto, 1986). Taylor (1969) describes organic matrix within second-order prisms that subdivides them into smaller units (in this study referred to as third-order prisms). Growth lines appear as concentric lines cutting perpendicularly across first-order prisms, and in most cases also through second-order prisms.

The crossed acicular subtype of the homogeneous ultrastructure (Shimamoto, 1986) occurs in several mollusc species, but is only comprehensively described previously for the marine gastropod *Cuvierina*. It is organized into single lamellae that are arranged into bundles intersecting at angles of 120-150° with dipping angles of 30 to 40° relative to the inner shell surface (Carter, 1989).

2 Materials and Methods

2.1 Aquaculture and Labelling Experiments

The “common cockle” or “ridged venus” *Katelysia rhytiphora* (Lamy, 1935) is a temperate, shallow burrowing species that occurs along the shorelines of Tasmania and South-Eastern to South-Western Australia (Edgar, 2000). Some species of this genus (*K. peronei*, *K. rhytiphora* and *K. scalarina*) are valued seafood, hence, *K. rhytiphora* can be successfully grown in aquaculture and husbandry protocols are available.

Specimens for this study were live-collected at Port Lincoln, South Australia and transferred into 50 litre polyethylene tanks at the seawater facility at Macquarie University with a stocking density of 14 bivalves per tank. All tanks were connected to a recirculating seawater system with continuous filtered and sterilized natural seawater supply. Water chemistry, salinity, pH and temperature resembled local ocean values. Polyethylene boxes (20-40 cm^2 and 10 cm height) filled up to ca. 9 cm with sterilized beach sand (boiled 60 min prior to use) allowed the bivalves to burrow. This setup enabled easy and quick transfer of the cockles between the larger tanks, thus minimizing handling stress. Indeed, the bivalves were observed to continue filter-feeding while being transferred, which is a reliable sign for the absence of handling stress. Acclimatization period was 3 weeks and experiments lasted 36 days. A 12h/12h day/night light cycle was maintained throughout the experiment. Cockles were fed daily with a mix of microalgae “Shellfish Diet 1800” (Reed Mariculture Inc., USA) containing *Isochrysis sp.*, *Pavlova sp.*, *Tetraselmis sp.*, *Chaetoceros calcitrans*, *Thalassiosira weissflogii*, and *Thalassiosira pseudonana*. Over the experimental period, bivalves were transferred twice after 12 days at normal seawater chemistry (ca. 8 $\mu\text{g/g}$ Sr) to labelling seawater chemistry at 18x mean ocean water average of 144 $\mu\text{g/g}$ Sr (3.5 g $\text{SrCl}_2 \cdot 6\text{H}_2\text{O}$ in 8 l seawater) where they remained for 6 days before being transferred back. These labelling periods are referred to as “Labelling Events”, LE1 and LE2, whereas periods with ambient Sr concentrations are referred to as “Normal Events”, NE1 and NE2. During labelling conditions, the water was homogenized using an airstone and water quality was maintained by fully renewing the labelled seawater every 48 hours. After the final labelling experiment, half of the population was collected from unlabelled seawater after 6 days and 12 days,



respectively, and deep-frozen at -20°C . After thawing and removing of soft tissues, shells were rinsed in deionized water and air-dried.

2.2 Sample Preparation

Valves were cut along maximum growth axis using an IsoMet low speed precision sectioning saw (Buehler, IL, USA). Left valves were mounted in round 1 inch mounts using EpoFix epoxy resin (Struers, Australia), while 3 mm thick shell slabs from right valves were fixed on microscopy glass slides using metal bisphenol-A-epoxy resin (Permatex, Hartford, CT, USA). After curing at room temperature, sample surfaces were ground and polished in steps using sandpaper (400–2000 grit) as well as 3 and $1\ \mu\text{m}$ diamond pastes. Left valves were further polished using a final chemical polishing step with a diluted suspension of colloidal silica ($0.05\ \mu\text{m}$) on a neoprene polishing cloth to ensure optimum conditions for high resolution analyses. Some shell pieces were immersed in a solution of 1% wt./vol. ethylenediaminetetracetic acid disodium salt dihydrate (EDTA; Sigma-Aldrich), ultrasonicated for 6 minutes, rinsed with Milli-Q water and air-dried. For SE-images unetched broken shell pieces and some etched with EDTA (1% wt./vol) were mounted on aluminium stubs using carbon glue, and gold-coated.

2.3 Optical Microscopy

A Leica M205C binocular stereomicroscope with reflective light was used to image shell slabs at 4x magnification along the entire shell cross-section. Images were stitched and contrast improved in Adobe Photoshop CS5. To obtain greyscale line profiles, the outer prismatic shell layer was cropped and further improved in contrast. Greyscale line profiles were acquired using ImageJ (Schindelin et al., 2015).

2.4 Electron Probe Micro Analyser (EPMA), Field Emission Gun Scanning Electron Microscopy (FEG-SEM) and Electron Backscatter Diffraction (EBSD)

Quantitative wavelength-dispersive X-ray spectroscopy (WDS) was carried out using a JEOL JXA 8200 Electron Probe Micro Analyser (EPMA) at the University of Mainz, Germany, with a defocused beam in rastering mode at 20,000 magnification to obtain concentrations of Na, Mg, P, S, Cl, K, Ca, Mn, Fe, Sr, and Ba calibrated against a variety of minerals and synthetic reference materials (Table S1). Backscattered electron (BSE) images at lower magnification were acquired from carbon-coated polished cross-sections. Specimens were imaged with 15 kV acceleration voltage and 8 nA beam current at 11 mm working distance. Epoxy mounts and broken pieces of shells were imaged with Field-Emission Gun Scanning Electron Microscopes (FEG-SEM), namely a JEOL JSM- 7100F and a Phenom XL at Macquarie University (BSE images at 15 kV and 8 nA), and a ZEISS Leo 1530 at the Max Planck Institute for Chemistry, Germany, for Secondary Electron (SE) images (at 3 kV and 2 nA).

Electron Backscatter Diffraction (EBSD) data were acquired at Oxford Instruments NanoAnalysis, High Wycombe, United Kingdom, using a Hitachi SU70 FE-SEM equipped with an Oxford Instruments AZtec 3.4 EBSD-EDS system, with an X-Max $150\ \text{mm}^2$ EDS detector and a CMOS-based Symmetry EBSD detector. Three EBSD maps were collected along the



axis of maximum growth in different regions of interest using 15 kV accelerating voltage, a beam current of 10 nA and a step size of 0.1 μm . The EBSD pattern resolution was 156 x 128 pixels at a collection rate of 195 patterns per second. Noise reduction was performed using the HKL software and datasets were processed using the MTEX toolbox in Matlab (Bachmann et al., 2010) following the protocol in Henry et al. (2017).

5 2.5 Micro-Raman Spectroscopy

Raman spectra were recorded at room temperature using a Horiba Jobin Yvon LabRAM HR Evolution spectrometer coupled to an Olympus optical microscope with the laser beam path aligned through the microscope objective (quasi-backscattering configuration). A diode-pumped solid state laser with 473 nm (~ 15 mW at sample surface) and a He-Ne laser with 633 nm (~ 10 mW at sample surface) excitation wavelength was used. Spectra recorded in the red spectral range ($\lambda_{\text{exc}} = 633$ nm) have a spectral resolution of 0.8 cm^{-1} and a pixel resolution of 0.3 cm^{-1} ; those recorded in the blue spectral range ($\lambda_{\text{exc}} = 473$ nm) have a spectral resolution of 1.6 cm^{-1} and 0.6 cm^{-1} pixel resolution using a grating with 1800 lines /mm.

Hyperspectral images were obtained using a software-controlled x-y table and a step width of 0.6 μm . All instrument set-up parameters and measurement conditions were strictly kept constant during automated point-by-point spectra acquisition to guarantee subtle changes of Raman band parameters to be recorded reliably. In the following, minute modification of Raman band parameters as obtained from hyperspectral mapping were interpreted qualitatively only. Data reduction includes background subtraction and peak fitting using Lorentzian-Gaussian (pseudo-Voigt) function. All FWHM values were corrected for the instrumental apparatus function using the empirical correction published in Váczi (2014).

2.6 NanoSIMS Analyses

Epoxy mounts were gold-coated prior to introduction into a new generation CAMECA NanoSIMS 50L ion probe equipped with a Hyperion RF plasma oxygen ion source, at the University of Western Australia. The primary oxygen ion beam was focused to a diameter of 100 nm and images were acquired from $100 \times 100 \mu\text{m}^2$ areas at a resolution of 1024×1024 pixels with a dwell time of 3.6 ms/pixel. ^{24}Mg , ^{40}Ca , and ^{88}Sr were measured on electron multipliers at a mass resolving power of 5000. The imaged areas were pre-sputtered at a slightly larger map area prior to acquisition. Images were processed using the OpenMIMS plugin for ImageJ/FIJI, where a correction for detector dead time was applied and the ratio of $^{88}\text{Sr}/^{40}\text{Ca}$ has been expressed as a Hue-Saturation-Intensity (HSI) colour scale – min (blue) = 10, max (magenta) = 100).

2.7 Thermal Gravimetric Analysis (TGA)

The inner and outer layer of a *K. rhytiphora* shell were separated with a DREMEL tool and mechanically cleaned. Both layers were soaked in H_2O_2 (Merck KGaA, Darmstadt; Germany) for 1 hr at room temperature and washed with Milli-Q water. After air-drying, each layer was powdered using an agate mortar and pestle. Total amounts of organics were determined with a TGA 2050 thermogravimetric analyser (TA Instruments, USA). About 10 mg of powdered sample was measured (two replicates). The analysis was carried out under a nitrogen atmosphere, at a linear heating rate of $10^\circ\text{C}/\text{min}$, between 25– 1000°C .



3 Results

3.1 Ultrastructure and Growth

The shell of *K. rhytiphora* consists of an inner crossed acicular layer and an outer compound composite prismatic ultrastructure covered by a very thin periostracum visible only in SEM (see subchapter 3.4). The outer layer is mainly responsible for shell extension, while thickening of the shell is achieved mainly by growth of the inner layer (Fig. 1C). The shell surface shows prominent, concentric ridges (Fig. 1A) and a yellow and purple to brown pigmentation on the inside (Fig 1B). Both layers are fully aragonitic (Fig. S1).

Cross-sections of *K. rhytiphora* shells are characterized by three dark bands at the ventral margin area (Fig. 1C, red box and detailed in Fig. 1D and E). These dark bands represent growth in warm waters during Australian summers months (~ August to April) in agreement with previous studies on other bivalve species (Carré et al., 2005; Soldati et al., 2008). A minor dark band at the very tip of the shell corresponds to the growth period in late November when the bivalves were sacrificed (Fig. 1C, red box and detailed in Fig. 1D and E). A greyscale line profile of the ventral margin area (Fig. 1C, red box and Fig. 1D) shows troughs that accurately correlate with 48 out of 50 spring tides at full moon (light grey, Fig. 1D) and new moon phases (dark grey Fig. 1D). Hence, this shell section was deposited within two years. Intervals between grey-shaded areas in Fig. 1D correspond to neap tides. This growth pattern is in accordance with findings that shell deposition is strongly influenced by tide conditions, whereby neap tides result in wider, lighter coloured increments in bivalve shells (Rhoads and Lutz, 1980; Schöne et al., 2002; Carré et al., 2005; Carré et al., 2006). Hence, *K. rhytiphora* shells show a well-defined fortnightly resolution in the most recent parts of the shell.

Micro-growth bands at the outermost shell tip (Fig. 1D, red box) can be correlated with tides from mid-August to mid-September 2016 at Port Lincoln, South Australia where the bivalves were collected (Fig. 1E, black dashed lines). This shows that these bands formed during one month from mid-August to mid-September 2016. This period is prior to when the bivalves were obtained at Port Lincoln and transferred to aquaculture conditions in mid-September. At this time, the line profile stops correlating with tides (blue shaded area in Fig. 1D, E). Shell increments formed during aquaculture (blue shaded area in Fig. 1D, E) consist of very dark growth increments and most likely reflect lower than normal growth rates. We observed the same patterns on two other specimens (not shown).

3.2 Validation of Sr-Incorporation

Incorporation of higher Sr-concentrations during labelling experiments was studied using NanoSIMS mapping and EPMA-based WDS analyses. Qualitative NanoSIMS mapping revealed two distinct bands of elevated Sr concentration in the outer layer directly at the ventral margin (Fig. 2A) as well as in the inner layer ca. 0.5 mm away from the ventral margin (Fig. 2B). Overlays of NanoSIMS maps with BSE images verify that light greyscales are caused by higher concentrations of Sr.

EPMA-based WDS spot analyses (Table 1) show elevated Sr contents of ≥ 2.3 wt.% SrO for the outer and 1.4 wt.% SrO for the inner structure. Strontium concentrations in growth regions from either before aquaculture (pre-aqua), during



acclimatisation (pre-LE 1) or between labelling events (NE 1) are around 0.2 wt.% (Table 1). Other major and minor element concentrations (Na, Mg, S, Cl) were identical within uncertainty between labelling and non-labelling experimental conditions. Concentrations of Mn, Ba, P, K, and Fe are below detection limits.

3.3 Raman Spectroscopy

5 Raman spot analyses show peak positions characteristic for aragonite (Fig. S1), namely a doublet at 701 and 705 cm^{-1} (ν_4 , CO_3 in-plane bending), a peak at 1084.8 cm^{-1} (ν_1 , CO_3 symmetric stretching), and several intrinsic bands between 170 and 300 cm^{-1} (Urmos et al., 1991; Wehrmeister et al., 2010). In addition, broad peaks centred at 1134 and 1532 cm^{-1} represent C-C single bond (ν_2 stretching mode) and C=C double bond (ν_1 stretching mode) of polyene chains in organic pigments (Otter et al., 2017).

10 Micro-Raman hyperspectral mapping of the most intensive peak at 1084.8 cm^{-1} revealed that band widths (full-width at half-maximum, FWHM) differ between Sr-labelled and unlabelled areas (Fig. 3). Two regions with systematic peak broadening are observed for both ultrastructures and correspond to the light greyscale Sr-labels in BSE images and depict the concentration change from 2.3 wt.% SrO in labelled to 0.2 wt.% of unlabelled shell. Although Sr concentrations in the water and duration of labelling conditions were identical in all labelling periods, the more recent outer label (LE 2) is narrower and
15 brighter than in the earlier label (LE 1) reflecting different shell growth rates. Band width distribution shows distinct narrow increments within both labels. Highest FWHM values within both labelled areas are 2.2 and 2.7 cm^{-1} for the outer (Fig. 3A) and 1.8 and 2.4 cm^{-1} for the inner layer (Fig. 3B, Table S2). In unlabelled areas FWHMs do not exceed 1.8 cm^{-1} . The difference in FWHMs of the ν_1 symmetric stretching band between labelled and unlabelled areas is typically about 0.5 cm^{-1} for both
20 structures. Further, the ν_1 symmetric stretching band shows a shift in peak position to lower wavenumbers in areas of high Sr concentration (Fig. S2, Table S2). Note, however, that FWHMs and peak positions do not vary among different textural features of the unlabelled shell architecture, and hence, may not be influenced significantly by grain size effects.

3.4 Architecture of the shell layers

3.4.1. The outer compound composite prismatic layer:

25 First-order prisms between umbo and ventral margin form a fan-like arrangement and the ridged outer surface as visible in radial sections of the outer shell layer shown in Fig. 4A (Taylor, 1969; Popov, 1986; Shimamoto, 1986). Potential 3D, out-of-plane bending of these prisms as described by Taylor (1969) and Popov (1986) may not be observed from two-dimensional cross-sections as shown here (Fig. 4A, Fig. S3). This arrangement produces a fan-like divergence of prisms in radial sections between umbo and ventral margin. Bending of the prisms outside the sectioning plane challenges measurement of individual
30 first-order prisms. However, Fig. 4A shows that first-order prisms originate and end at the prominent organic-rich growth checks (identified by their dark greyscales) and can reach sizes of $>700 \mu\text{m}$. This species develops annual growth checks (Fig.



4A, blue arrows), which are distinctive features in the shell marking periods of strongly reduced shell growth. Growth checks can be organic rich as observed here or comprise a different morphology such as a thin layer of prisms (see below and Ropes et al. (1984)). In contrast to previous studies that have reported first-order prisms to exhibit square shapes in longitudinal cross-sections (e.g., Taylor, 1969), we found irregular hexagonal prism cross-sections (Fig. S4). Our measured widths of around 17
5 μm are similar to literature values of around $10 \mu\text{m}$ for other venerids (Shimamoto, 1986). Lengths and widths result in aspect ratios of >40 , individually enveloped by organic sheaths visualized by dark greyscales in Fig. 4A. On the outside the shells are covered by a ca. $1 \mu\text{m}$ thin organic periostracum (blue arrows, Fig. S3).

First-order prisms consist of second order prisms arranged radially around their central axis with angles of 68° in between opposing second-order prisms (Fig. 4B, Fig. S5). Individual second-order prisms have minimum lengths and widths
10 of $3 \pm 0.3 \mu\text{m}$ and $0.3 \pm 0.06 \mu\text{m}$ ($n=8$), respectively, with aspect ratios of 10. Although no lengths are provided in the literature, the widths are in very good accordance with values provided by Shimamoto (1986) for the shells of other venerids. The angle of 68° between two facing second-order prisms gives rise to the feathery arrangement of second-order prisms in cross-sections that we observed in *K. rhytiphora* and that has been described previously (Shimamoto, 1986; Popov, 1986). Both first- and second-order prisms were found to be enveloped by organic sheaths (Fig. 4A, B, Fig. S4) supporting literature findings for this
15 shell structure in molluscs (Taylor, 1969; Shimamoto, 1986).

Second-order prisms consist of third order prisms (Fig. 4C), which are arranged with their long axis parallel to each other (Fig. S6). They have lengths of $496 \pm 129 \text{ nm}$ and widths of $67 \pm 16 \text{ nm}$ ($n=8$) with an aspect ratio of 8 that is lower compared to first- and second-order prism. The smallest building blocks revealed by SEM images are nano-granules with sizes in the range of 70 nm in shell samples that were etched (Fig. 4E and F).

20

3.4.2. The inner crossed acicular layer:

The acicular-prismatic boundary is marked by a ca. $30 \mu\text{m}$ wide transitional layer of granular texture comprising high numbers of short first-order prisms and spherulitic grains (Fig. S3). The growth check, which is organic-rich in the outer layer, continues as a thin prismatic layer into the crossed acicular structure (Fig. 4A, green arrow). Bundles of cross-layered lamellae
25 in the inner shell layer are enveloped by organic sheaths (dark grey, Fig. 4D) and measure up to $1.4 \times 0.8 \times 0.2 \mu\text{m}$ (Fig. S8). Individual acicular lamellae are $1.8 \pm 0.4 \mu\text{m}$ long and $0.22 \pm 0.05 \mu\text{m}$ ($n=19$) wide with aspect ratios of about 8 (Fig. 4D, Fig. S7). Angles between acicular lamellae are $81 \pm 8^\circ$ ($n=6$). Etching of the inner layer also revealed a nano-granular texture (Fig. 4F).



3.4.3. Organic content:

Thermal gravimetric analysis (TGA) was used to determine the total amount of organic macromolecules in the shell, which amounts to 1.42 ± 0.03 wt.% and 2.19 ± 0.04 wt.% for the inner and outer shell layer, respectively. The organic phases are visible after etching the mineral phase and exhibit fibre- and sheet-like textures (Fig. 4E, F).

5 3.5 Crystallographic Preferred Orientations

The microstructure of the aragonite crystals in the outer and inner shell layers is shown in the orientation map in Fig. 5A. The map is colour-coded using an inverse pole figure colour scheme, showing the crystal direction aligned with the horizontal direction in the orientation map (i.e. parallel to the growth direction). Blue, green, and red indicate an alignment of the crystallographic a- [100], b- [010], and c-axes [001], respectively. The predominance of red color shades indicates that there is a strong crystallographic preferred orientation (CPO), with the c-axes [001] well aligned parallel to the growth directions of both layers. As previously described above, we observe second-order prisms also in the orientation map to appear feathery arranged within first-order prisms (some first-order prism are outlined in green in Fig. 5A). The rims of the first-order prisms in the outer shell layer are well resolved in the orientation map, while most of their cores remains dark and unindexed: this is indicative of poor or non-existent diffraction patterns as measured during the EBSD indexing cycle. We believe this effect arises mainly from the overall geometry of the polished surface across second-order prisms that are orientated almost vertically in these areas. These prisms are likely removed to some extent during polishing creating topography that challenged EBSD signal generation. A lower crystallinity in these areas is excluded as this would have been visible in Raman maps (Fig.3, Fig. S2). The inner crossed acicular shell layer shows ca. $17 \mu\text{m}$ by ca. $10 \mu\text{m}$ large areas of lamellae, where the aragonite crystallographic axis are well co-orientated (Fig. 5A, yellow outlined) and share high amounts of crystallographic twin boundaries.

Pole figures (Fig. 5B) show a strong preferred orientation of the aragonite c-axes perpendicular to the growth layers in the inner crossed acicular shell layer. The crystallographic a and b axis form a plane of random orientations parallel to the growth lines in the inner crossed acicular layer and perpendicularly to the direction of shell thickening (DOG Cr Ac, Fig. 5B). Aragonite c-axes in the outer shell layer align with the direction of shell extension (DOG Pr., Fig. 5B), which is at an angle with that of the inner shell layer. We identified high abundance of twinning with 46% (outer layer) and 56% (inner layer) of the grains showing at least one twin (i.e. $63.8^\circ \pm 5^\circ$ rotation around the 001 axis) for the outer and inner layers, respectively.

3.6 Calcification Rates

The Sr-labels are easily recognizable (Fig. 4A) in both the prismatic and the crossed acicular layers (Table 2). Due to the geometry of first order prisms without- and inward bending in cross-sections, we decided to provide growth rates as calcification rates for the outer layer instead of the dominating macroscopic direction of dorso-ventral shell extension (e.g. Gillikin et al., 2005; Carré et al., 2006). Calcification rates for the inner layer are measured parallel to the growth direction



(thickening) of this layer. Table 2 gives the average growth rates for all experimental intervals (Sr-enriched and ambient non-labelled) during aquaculture. Length measurements in sectional images were replicated thrice with ImageJ at five different locations along cross-sections through the maximum growth axis (Figs. S13, S14 and Tables S3, S4).

Although sizes and ages of the used bivalves are similar, growth rates are found to be heterogeneous across the population, especially for the outer shell layer (Fig. 6A-B). The labelled layer LE1 grew $5.6 \pm 0.9 \mu\text{m}$ on average (range: 2.2 – 13.3 μm) and layer LE2 grew $3.6 \pm 0.7 \mu\text{m}$ on average (range: 2.6 – 4.8 μm) within 6 days of Sr-labelling procedure (Table 2). Between both labelling intervals a 12-day ambient period (NE1) resulted in additional growth of $12.2 \pm 1.1 \mu\text{m}$ (range: 3.7 – 22.3 μm). In comparison, the inner, crossed acicular shell layer grew only $5.3 \pm 0.6 \mu\text{m}$ average (range: 3.5 – 7.0 μm) during LE1 and $4.3 \pm 0.3 \mu\text{m}$ (3.7 – 5.5 μm) during LE2. Twelve days of ambient conditions during NE1 resulted in $9.0 \pm 0.5 \mu\text{m}$ (3.7 – 13.6 μm) of growth (Table 2). Despite these variations, average daily growth rates suggest the outer structure to grow 17 % faster than the inner structure, which grows steadier but more slowly (Table 2). Also, rates tend to decrease effectively with increasing distance to the ventral margins (Fig. 4A). Individual Sr-labels comprise different narrow increments of varying width and greyscale intensity in both types of ultrastructures (Fig. 4B, D). Systematic shift towards faster or slower growth rates during Sr-incubation was not observed (Fig. 6C).

15 4 Discussion

4.1 Multiscale Architecture

Compared to aragonitic or calcitic simple prisms associated with the nacropismatic structure of e.g. *Pinna*, *Mytilus*, *Pinctada* or *Hyriopsis* bivalve species, the aragonitic compound composite prismatic ultrastructure of *K. rhytiphora* with three prismatic orders is far more complex (Jacob et al., 2011; Fitzer et al., 2015; Hovden et al., 2015). The sizes of these units range over multiple length scales from mm (first-order prisms) to nm (third-order prisms) (Fig. 4A-C, Fig. S11). Regarding the number of differently sized units as well as their approximate size range, the compound composite prismatic structure shares more similarity with the crossed-lamellar ultrastructure than the simple prism structure associated with nacropismatic shells (Agbaje et al., 2017b). In *K. rhytiphora* the first order prisms run perpendicular to the growth checks and radially with respect to the radial cross-section (Fig. 4A) and comprise two orders of acicular prisms with high aspect ratios that are arranged feathery (radially around the central prism axis in 3D) in the case of second-order prisms and parallel in the case of third-order prisms (Fig. 4B, C).

We show here that units of all prismatic orders as well as each lamella in the crossed-acicular structure are enveloped by an organic sheet with a total organic content of 2.2 wt.% in the outer and 1.4 wt.% in the inner layers (Fig. 4E-F, Fig. S9). Organic contents of both shell layers of *K. rhytiphora* take intermediate positions between nacropismatic shells with their thick, well-defined interlamellar membranes and high 3-5 wt.% total organic content on one side and the highly mineralized crossed-lamellar shells with less than 1 wt.% organic content on the other (Agbaje et al., 2017a).



Second-order prisms in the outer shell layer are co-oriented across their thin organic envelopes and crossed acicular lamellae show epitaxial orientation over 10 μm (Fig. 6A, Fig. S10). Similar co-orientation has been observed in nacre and in crossed-lamellar shells (e.g. Gilbert et al., 2008; Agbaje et al., 2017b). In the case of nacre, epitaxial growth of new aragonite tiles across thick interlamellar membranes is maintained by 150-200 nm wide mineral bridges (Checa et al., 2011). In *K. rhytiphora* shells the organic sheaths around architectural units are significantly thinner than the interlamellar membranes in nacre (~30 nm), indicating that mineral bridges are not critical for growth and co-orientation in non-nacreous shells.

The inner crossed-acicular ultrastructure is built less complex than the outer prismatic structure and consists of only two architectural orders: firstly, cross-layered individual lamellae of a few microns in length that are angled to each other at approx. 80° and have dipping angles of <20° towards the inner shell surface. These lamellae appear grouped to form second-order architectural units of cross-layered bundles in SE images (Fig S8). Equal-sized bundle-like arrangements of crossed acicular lamellae were also observed by Carter (1989) in the marine gastropod *Cuvierina*, but these show larger horizontal angles in combination with smaller dipping angles than those observed in this study. These deviations are, however, considered marginal and likely reflect species-dependent variations as those described for crossed-lamellar mollusc shell structures (Almagro et al., 2016). In orientation maps of the inner layer, we observed areas of co-orientated lamellae that show strong internal co-orientation (Fig. 5A and Fig. S12, yellow outlined) that might resemble pseudo-prisms (e.g. Pérez-Huerta et al., 2014). The stack-wise arrangement of crossed acicular lamellae in *K. rhytiphora* contrasts with the crossed-lamellar structure of other bivalves, which shows only random orientation of a- and b-axes in a girdle around the c-axis, while the c-axis is identically orientated parallel to the DOG in both shells (Almagro et al., 2016; Agbaje et al., 2017b). Similarly, the c-axis [001] in nacreous shells is orientated parallel to the growth direction. Nacre platelets vary ~30° in orientation around the c-axis and show a strong vertical alignment for all crystallographic axes of stacks of up to 10 tablets (Feng et al., 2000; Olson et al., 2013).

A prominent structural motif of aragonitic bivalve shells is the generally high amount of crystallographic twinning. In *K. rhytiphora* we observed 46 % and 56 % aragonite twin boundaries in the outer and inner layer, respectively. These numbers are similar as amounts reported for crossed-lamellar (26%) and nacreous (20-65%) structures (Chateigner et al., 2000; Agbaje et al., 2017b). It has to be noted that aragonite twinning in bivalve shells is also present at the nano-scale (Kobayashi and Akai, 1994) and, thus, values given here are minimum values, because they are a function of the spatial resolution of the EBSD analyses.

The smallest mineralized unit of both ultrastructures are granules with sizes of tens of nanometres (Fig. 4E). Although the compound composite prismatic ultrastructure differs significantly in the mm-to μm range from other bivalve structures, these features are similar in size to the nano-granular texture observed in nacropismatic and crossed-lamellar shell samples and are considered a common motif for bivalve shells (Jacob et al., 2008; Jacob et al., 2011; Wolf et al., 2012; Böhm et al., 2016; Wolf et al., 2016; Agbaje et al., 2017b). Previous studies showed that these granules are enveloped by thin, intergranular organic sheaths and most often result from non-classical crystal growth via Amorphous Calcium Carbonate (ACC) (Jacob et al., 2008; Jacob et al., 2011; Wolf et al., 2012; Younis et al., 2012).



4.2 Mechanical Properties

The mechanical properties of shells i.e. stiffness, impact resistance, and toughness outcompete monolithic aragonite by several magnitudes as the mechanical performance of the latter is compromised by its high anisotropic elasticity (Villiers, 1967; Jackson et al., 1988; Wang et al., 2001; Katti et al., 2006). Bivalve shells improve their mechanical properties through different strategies including their highly hierarchical organization across several length scales, high amounts of crystallographic twinning, nano-granularity, and the intimate arrangement of mineral and organic phase (e.g. Barthelat et al., 2006). These strategies aim to minimize anisotropy and have been developed through evolutionary fine-tuning (Weiner et al., 2000). An important measure for the mechanical performance of materials is the Young's modulus, which describes the stiffness of a material in response to stress and strain (Hashin, 1962). Young's moduli for *K. rhytiphora* were calculated based on EBSD data and the elastic constants of the mechanical performance of aragonite single crystals (Pavese et al., 1992). All EBSD data (Fig. 5, Figs. S10, S12) were used to maximize the analysed dataset and to obtain Young's moduli separately for both ultrastructures as well as for the bulk shell (Fig. 7). We report maximum values of 111 GPa for the inner, 105 GPa for the outer layer and 109 GPa for bulk shell with all values in the range of those reported for crossed-lamellar and nacre (e.g. Fitzner et al., 2015; Agbaje et al., 2017b). Stereographic visualization reveals a girdle-like arrangement of elastically stiffer orientations that result in quasi-isotropic planes perpendicular to the growth direction (Fig. 7), similar to observations of Agbaje et al. (2017b) for crossed-lamellar shell of *Tridacna derasa*. Hence, *K. rhytiphora* demonstrates exemplarily how bivalves employ strategies to minimize anisotropy and, thus, optimise their mechanical properties and protective function.

4.3 Growth Dynamics and Biomineralization

On average, both shell layers have grown 28.4 μm (outer) and 24.2 μm (inner) over the duration of the experiment (Table 2). Although we show that the outer layer grows faster on average, growth rates vary significantly among the different experimental periods, both within each individual specimen and across the whole population (Table 2, Tables S3, S4). The inner layer shows lower and more homogeneous daily growth rates ($0.73 \pm 0.07 \mu\text{m}$) compared to the outer layer ($0.85 \pm 0.11 \mu\text{m}$) (Table 2, Fig. 6). A higher growth rate for outer bivalve shell layers has been observed in previous studies (Carré et al., 2005; Foster et al., 2009). Growth rates of the inner layer are highest near the ventral margin (Fig. 4A) and decrease with distance from it.

Looking at growth features across all scales, we observe single first-order prisms to grow from one growth check to the next within a year (Fig. 4A, blue arrows). Second-order prisms with lengths between 3 and 6 μm (Fig. S5, see 3.4 *Architecture of the shell layers*) and crossed acicular lamellae grow at rates of days (Fig. S7) in our aquaculture experiment, while nanometre-sized third-order prisms form within hours (Fig. S6).

K. rhytiphora shells show ornamental ridges along the outside of their shells (Fig. 1) and it is an interesting question how and whether these ridges are related to shell growth. Specimen K2-04, that is characterized by homogenous, high growth rates allows us some insight into this issue: The ridge feature between the last two organic growth checks (Fig. 4A, area



between blue arrows) matches a growth time of 365 days (applying the growth rate of 13 $\mu\text{m}/6$ days from LE1). However, organic growth checks are not always associated with ridge features (Fig. 4A, purple arrow), as ridges are evenly distributed and relatively similar in width (Fig. 1C), resulting in a decrease in number of ridges per year as an ontogenetic effect. Our findings are in accordance with those of Radermacher et al. (2009), that the distinct surface ornamentation spines of the queen conch *Strombus gigas* are produced at different times across different individuals and suggested that these are genetically controlled rather than environmentally or seasonal. The highest growth rates in specimen K2-04 are associated with the beginning of a new ridge that starts as a fine protruding tip (Fig 4A, Fig. S15). Other specimens scarified at the same time, but showing higher growth rates, are observed to have just started producing their next ridge feature (Fig. S13D, E) and specimens with lower growth rates have not yet started producing the next ridge feature at that time (Fig. S13B, F). We suggest this correlation between fast growth rates and the newly-formed ridge feature may indicate a protective mechanism to thicken and support the delicate protruding tip of a new ridge.

Both Sr-labels LE1 and LE2 (Fig. 4A) in the outer layer consist of several narrow increments of varying bright grey areas caused by variations in Sr concentration (Fig. 2 and 3, Table 1). A greyscale line profile across LE1 (Fig. 4B) reveals six distinct peaks (Fig. S16A), which correlate with increments of higher growth during the six-day period spent in Sr-enriched conditions. One day is composed of one short bright and one longer dark increment. Feeding times as an explanation for the observed correlations are excluded based on the steady availability of food during labelling intervals. A similar pattern is observed in the line profile across the second labelling experiment LE2 (Fig. S16B), though the profile appears distorted because of an overall decreasing trend in growth rates especially in the latter half of the labelled band (Table 2, Fig. 6A). The narrow bright increments within the label are likely caused by higher growth rates and are in line with other studies (Gillikin et al., 2005; Carré et al., 2006). This correlation was explained by the growth entrapment model (Watson, 1996) that describes higher growth rates to coincide with higher concentrations of non-formula elements such as Sr or Mg that randomly substitute for Ca. We suggest a diel physiologically controlled variation of calcification rates as possible explanation of these small-scale variations.

Addadi et al. (2006) proposed a direct contact between mantle epithelium and growth front, thereby, opposing the idea of a significant volume of extrapallial fluid within this space (Rousseau et al., 2009). The extrapallial fluid in bivalves contains high concentrations of proteins with Ca^{2+} -binding properties that are thought to play an integral role in the calcification process (e.g. Cusack et al., 2008). BSE images of *K. rhytiphora* shells (Fig. 4A) show sharply defined changes between labelled and unlabelled areas. As the water was replaced fully at the start and end of the Sr-enriched incubations, these abrupt changes in Sr concentration in the shell indicate that physiological processes involving Sr incorporation into the shell have no lag and imply that the extrapallial fluid cannot be very voluminous. Hence, we interpret the mantle epithelium tissue as an effective ACC “factory” that records trace elemental changes immediately as they occur, which validates the significance of bivalve shells to record environmental changes with high resolution (e.g. Schöne et al., 2005).

A fundamental observation of this study is that the calcification front runs evenly across all structural units and architectural orders of the shell independently of the current growth rate. This is observed via higher magnification BSE images



that show the labels to cut across the different architectural building blocks (Fig. 4B, D) without showing a compartmentalized growth where the label would rather follow a zig-zag trend between fully labelled and unlabelled units. This is clearly visible from the sharply defined change between labelled and unlabelled shell areas (Fig. 4B and D), as well as from the cyclic variations in short-term growth rates (discussed above). Our results for *K. rhytiphora* thus supports models of calcification via directional solidification as recently proposed by Schoeppler et al. (2018). These authors suggest that the saturation states of shell-building constituents (and other parameters) at the calcification site are controlled by the mantle epithelium cells of the organism and that this physiological control produces the different polymorphs and architectural morphologies within the shell.

4.4 Revisiting the Concept of Ion Transport Pathways

Previous studies have proposed Ca to be transported across the mantle epithelium by different pathways: (1) Intracellular, active selective transport consuming Ca^{2+} -ATPase enzymes (Cohen and McConnaughey, 2003; Gillikin et al., 2005), (2) intercellular, diffusion driven, non-selective transport, and (3) intracellular, diffusion driven, selective transport (e.g. Klein et al., 1996). A precondition to all models is that Sr^{2+} and Ca^{2+} , due to nearly identical ionic radii and charge, are not discriminated (e.g. Sather and McCleskey, 2003).

We observed virtually identical enrichment factors for Ca and Sr ($\text{Ca}_{\text{Shell}}/\text{Ca}_{\text{Seawater}}$ and $\text{Sr}_{\text{Shell}}/\text{Sr}_{\text{Seawater}}$) in labelled and ambient conditions (Table 3). This suggests that Sr-ion transport is independent from concentration changes in the seawater. Such consistent enrichment factors would not be achievable using transport mechanism (1), as each ATPase-transported Sr ion would be at the expense of a Ca ion, which would be expected to dramatically increase Sr-enrichment during labelled conditions. In the case of transport mechanism (2), it should be expected that Ca/Sr ratios in the shell are identical to the variation in the seawater during controlled aquaculture. However, the Ca/Sr ratio of water in unlabelled conditions is 40/1 while measured values of Ca/Sr in unlabelled shell are 389/1 and shows a clear preference for Ca over Sr. The same high degree of preference is observed when comparing the Ca/Sr ratio of labelled water (4/1) with labelled shell (19/1). Hence, the strong enrichment of Ca from seawater to shell in both conditions strongly support selective transport process (3).

Our findings are in accordance with Carré et al. (2006), who showed that only pathway (3) can achieve ion fluxes high enough to sufficiently supply the calcification front. However, the proposed transport pathway across the mantle epithelium contradicts other findings that showed Ca to be transported as ACC-nanogranules to the calcification front (Loste et al., 2004; Addadi et al., 2006; Jacob et al., 2011; Zhang and Xu, 2013). We argue here that ion transport describes Ca transport into the mantle epithelium only prior to ACC formation and that this aspect of the model is therefore in line with non-classical crystallization processes in mollusc shell biomineralization (Jacob et al., 2011; de Yoreo et al., 2015; Wolf et al., 2016).

4.5 Limitations of Pulsed Labelling Experiments in Aquaculture Conditions

Our Micro-Raman maps demonstrate the impact of enriched Sr concentrations on the aragonite crystal structure. We observed peak broadening of ca. 0.5 cm^{-1} (Fig. 3) and position shift of ca. 0.5 cm^{-1} of the ν_1 symmetric stretching band towards lower



wavenumbers in Sr-enriched areas (Fig. S2, Table S2). The observed peak shift in the Sr-labelled areas is interpreted to result from slight changes in interatomic distances due to the incorporation of Sr on nine-fold coordinated Ca-sites in the aragonite crystal structure. Similar, chemically-induced effects on band position and width have been reported for e.g., the aragonite CaCO_3 to strontianite SrCO_3 solid solution (Alia et al., 1997), the calcite CaCO_3 to magnesite MgCO_3 solid solution (Bischoff et al., 1985), Sr substitution in apatite (O'Donnell et al., 2008), or monazite solid solution (Ruschel et al., 2012). All authors reported consistently, that extrinsic Raman bands shift to lower wavenumbers with increasing substitution of larger cations. Band-width broadening have been interpreted to result from structural disorder as caused by the incorporation of non-formula elements. Congruently, we observed the extrinsic ν_1 [CO_3] band to shift towards lower wavenumbers and to broaden with an increasing replacement of Ca (1.18 Å, ionic radius in 9-fold coordination) with Sr^{2+} (1.31 Å).

10 We, however, found no evidence for the formation of a separate i.e. clustered Sr-carbonate phase as the major ν_1 [CO_3] band of strontianite SrCO_3 , (at 1073 cm^{-1} ; Alia et al., 1997) was not detected. The latter interpretation is in accordance with earlier findings of Foster et al. (2009), who reported random substitution of Sr for Ca in aragonitic *Arctica islandica* shells, instead of Sr clustering as local strontianite or in the organic phase. These findings are further supported by our EBSD data (Fig. 6, Fig. S10, Fig. S12) that do not reveal any significant influence of Sr on the crystallographic orientations as well as by
15 the comparison of daily growth rates of Sr-labelled and unlabelled areas (Fig. 5C), that do not show a systematic change in growth increments during Sr-enriched periods.

While shell growth rates are clearly downscaled in our aquaculture experiment, we exclude a negative impact on the calcification processes. Hence, labelling experiments with a Ca substituting trace element offers the potential to study calcification processes down to the sub-micron range with excellent analytical detectability for a wide range of micro-beam
20 techniques and are superior to experiments with fluorescent markers e.g. Calcein that are limited in spatial resolution and, furthermore, are suspected to alter biomineralization processes in some biocalcifiers (Russell and Urbaniak, 2004; Thébault et al., 2006; Allison et al., 2011; Gorzelak et al., 2014).

Reduced growth rates in aquaculture conditions cannot be explained by ontogenetic trends alone but result from missing tidal cycles. *K. rhytiphora* belongs to the intertidal bivalve community for which a strong influence of tides on shell
25 growth is well known (Rhoads and Lutz, 1980; Schöne et al., 2002; Carré et al., 2005; Carré et al., 2006). Highest growth rates, observed in previous studies, formed during neap tides underline our argument that these species require higher water pressures for optimal shell growth (Carré et al., 2005; Carré et al., 2006).

5. Conclusion

Pulsed Sr-labelling experiments and correlated NanoSIMS, FEG-SEM and Raman mapping resolve growth rates at the
30 nanometre scale and show compelling potential to shed light on important aspects of growth dynamics in bivalve shells:

- The calcification front runs evenly across all structures and architectural orders as the Sr labels are observed to cut across the different hierarchical units of both layers, instead of showing compartmentalized growth.



- Narrow increments with variable Sr content within the labelled shell point towards cyclic metabolic activity during calcification.
 - Sharp transitions between labelled and unlabelled shell areas indicate that physiological transport processes for Sr have no significant lag and suggest that the extrapallial fluid cannot be very voluminous.
- 5
- Identical Sr-enrichment factors for labelled and ambient shell areas support models of ion transport via a passive selective pathway to the mantle epithelium followed by calcification via amorphous calcium carbonate.

Data availability.

All data can be accessed by email request to the corresponding author.

Author contribution

- 10 LMO and DEJ designed and coordinated the study. LMO conducted aquaculture experiments, sample preparation, and analyses. OBA, CL, and PH assisted with data collection. NanoSIMS and EBSD data were collected by MRK and PT, respectively. HH helped with EBSD data processing. LMO drafted the manuscript. All authors participated in writing the manuscript and gave final approval for publication.

Conflict of Interest

- 15 The authors declare that they have no conflict of interest.

Acknowledgements

- We acknowledge Michael W. Förster, Antje Sorowka, Steve Craven, and Jacob Byne for help and advice on sample preparation. Stephan Buhre is kindly thanked for calibrating the EPMA system. We thank the Macquarie University Faculty of Science and Engineering Microscope Facility (MQFoSE MF) for access to its instrumentation and support from its staff
- 20 members Sue Lindsay and Chao Shen. Jane Williamson and Josh Aldridge are thanked for access and assistance at the Macquarie Seawater Facility. Wayne O'Connor from Port Stephens Fisheries Centre, NSW Department of Primary Industries is thanked for insightful discussions on husbandry protocols. The authors received financial support through an Australian Government International Postgraduate Research Scholarship (IPRS) awarded to LMO, a Macquarie University Research Excellence Scholarship (iMQRES) awarded to OBA, and DEJ is supported via the Australian Research Council through a
- 25 Discovery Grant (DP160102081). C.L. gratefully acknowledge the use of instrumentation funded through an honorary-associate agreement with the ARC CFSS/GEMOC at Macquarie University, Sydney and financial support by the Austrian Science Fund (FWF), through project J3662-N19. The authors acknowledge Microscopy Australia, the Science and Industry



Endowment Fund, and the State Government of Western Australian for contributing to the Ion Probe Facility at the University of Western Australia.



Figures and Figure Captions

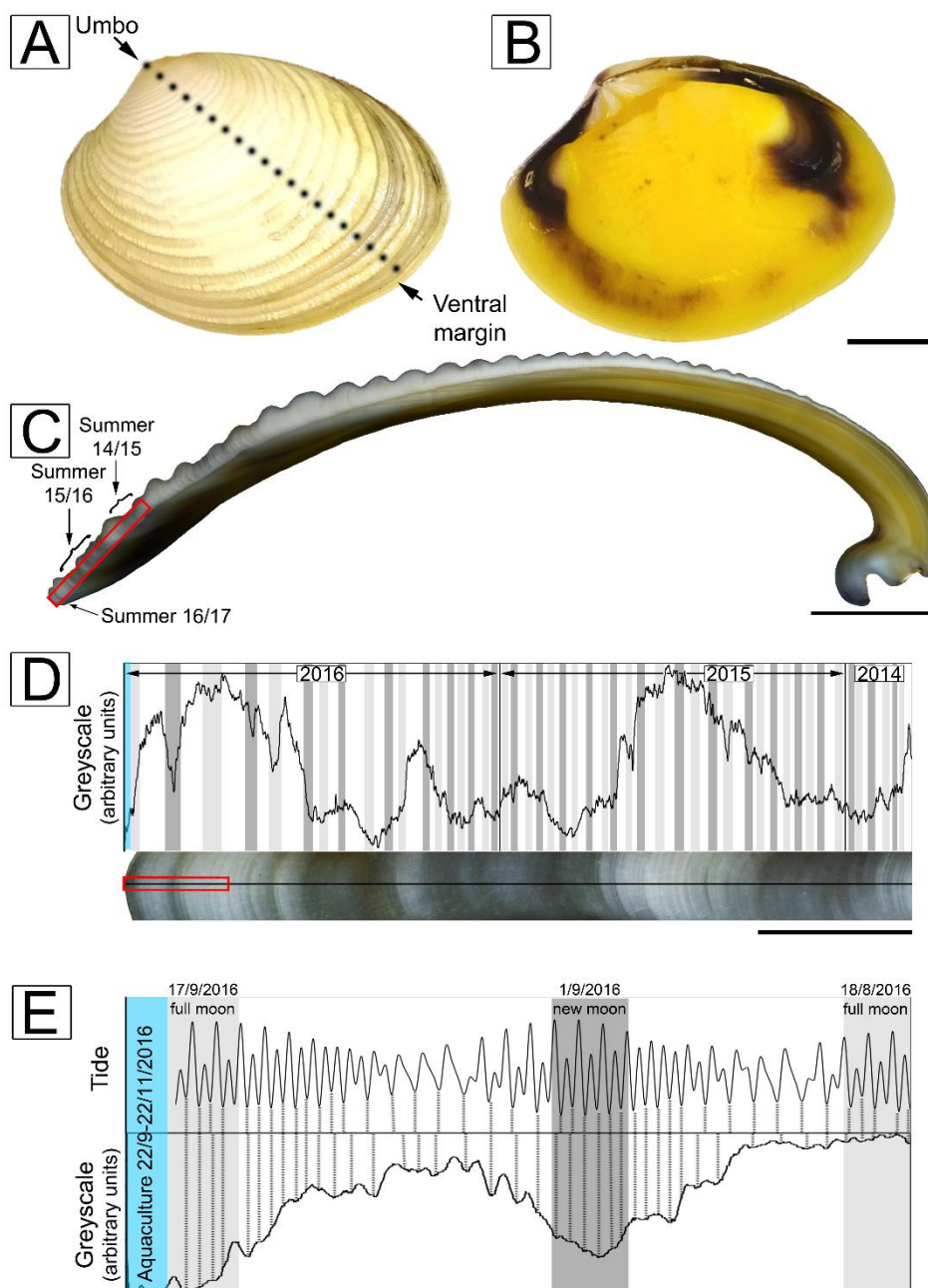
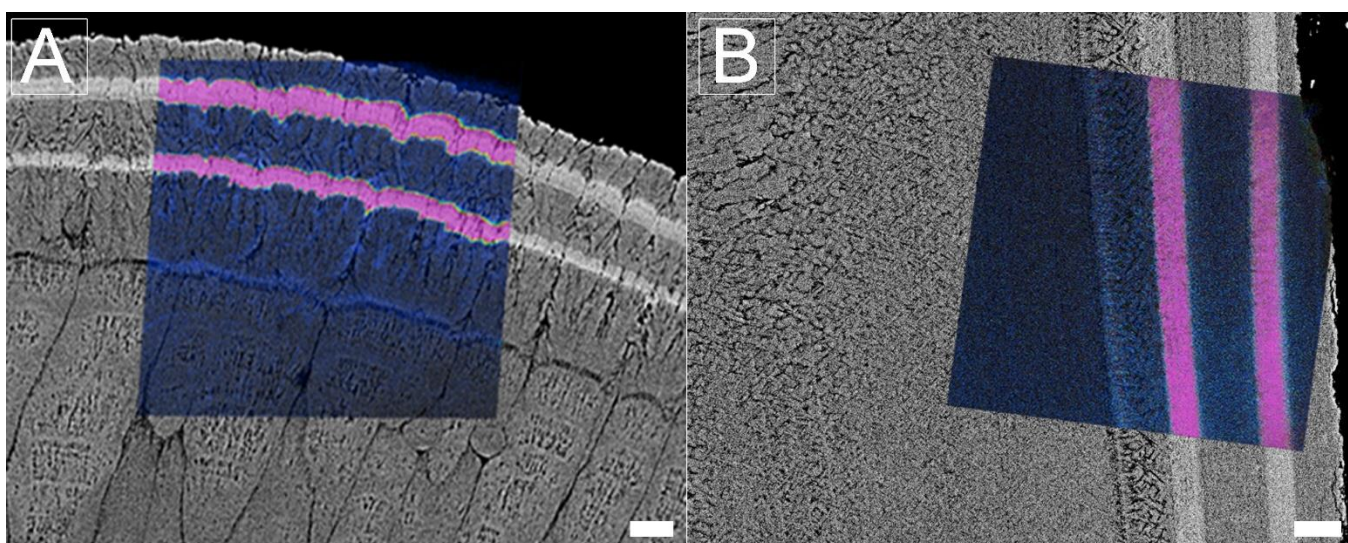


Figure 1: Outside (A) and inside (B) view of an unlabelled *K. rhytiphora* shell. Dashed black line in (A) indicates where the shell was sectioned. All cross-sections in this study are prepared as radial sections along the maximum growth axis unless otherwise specified. (C). Dark bands (arrows in C) are summer growth periods between lighter coloured winter periods and are magnified in D (red box in C) with a greyscale line profile. Distinct troughs in greyscale intensity correlate with 48 out of 50 spring tides in two



years from the collection site of the bivalves (full moon: light grey, new moon: dark grey) giving fortnightly growth resolution in this shell area. Greyscale line profiles (E) of the area marked by the red box in D shows the most recent shell growth increment in the wild (mid-August to mid-September 2016). In this part tides correlate with most shell increments (black dashed lines), while this correlation is lost after start of aquaculture (blue area). Blue area in D, E marks the aquaculture period with lower than normal growth rates. Scale bars are 10 mm (A-B), 5 mm (C), 1 mm (D), 0.1 mm (E).



10 Figure 2: FEG-SEM BSE images showing polished cross-sections of the outer (A) and inner (B) layers of a Sr-labelled *K. rhytiphora* shell (specimen ID: K2-06) overlain with NanoSIMS $^{88}\text{Sr}/^{40}\text{Ca}$ maps. Ambient seawater $^{88}\text{Sr}/^{40}\text{Ca}$ ratios are depicted in blue, while shell formed during Sr-enriched incubations are shown in pink. Scale bars are 10 μm .

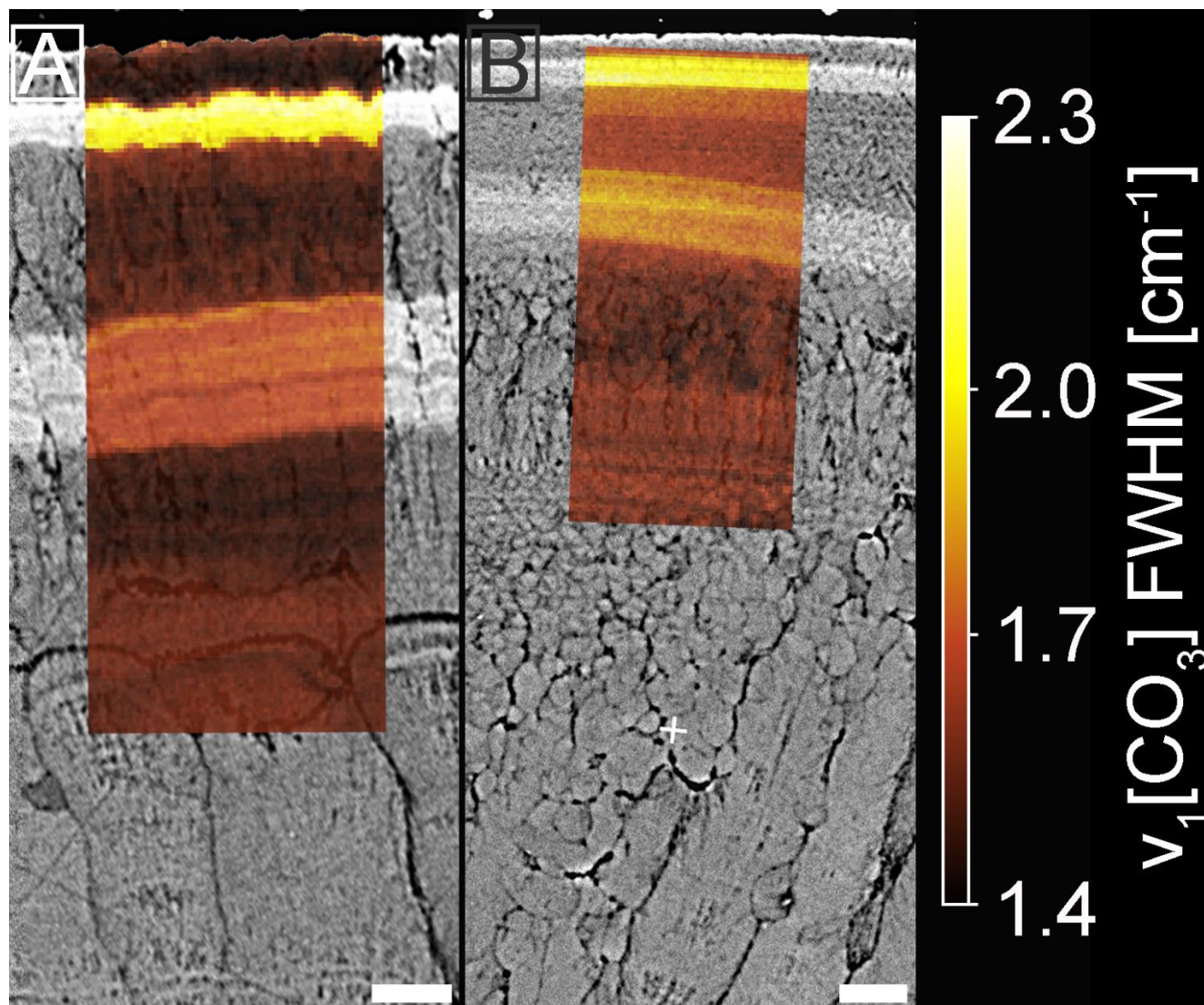
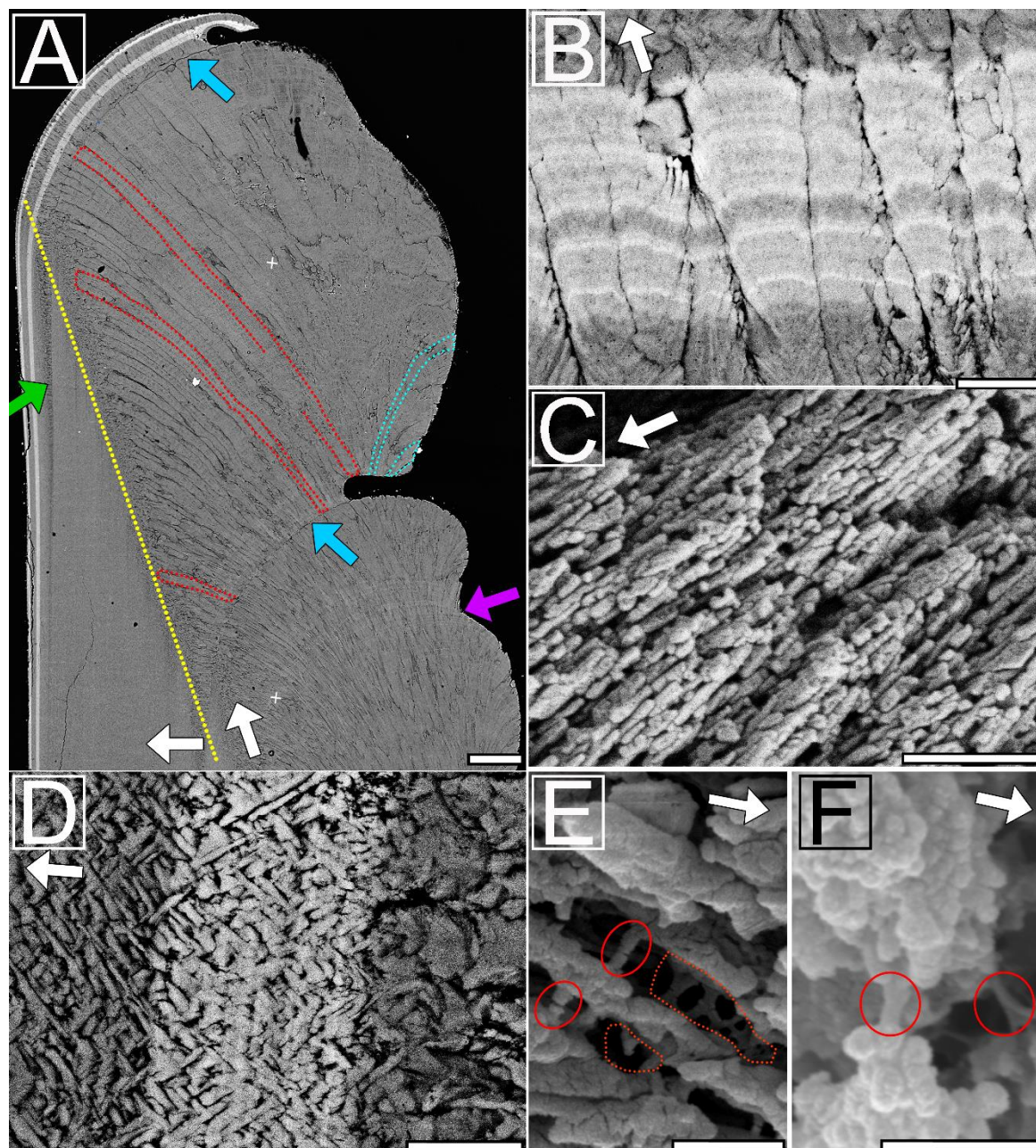


Figure 3: Micro-Raman maps (sample K2-04) showing the effect of Sr concentrations on the FWHM of peak ν_1 at 1084.8 cm^{-1} in the outer (A) and inner layer (B). Raman maps are overlain on BSE image. Bright grey-scale areas in the BSE images show elevated Sr-contents correlating with peak broadening (FWHM increase, see scale in cm^{-1}) in the labelled shell areas. For Micro-Raman maps of peak shifts see Fig. S2. All values are bandwidth corrected after Váczi (2014). Scale bars are 10 μm .



5 **Figure 4: Backscattered images showing cross-sections along the maximum growth axis of Sr-labelled *K. rhytiphora* shells: (A) shows the ventral margin of the shell. First-order prisms in the prismatic outer layer bend inwards (red outlined) reach lengths of up to 700 μm with widths of 17 μm . Outward bending prisms (blue outlined) form the ridged surface ornamentation of the shell. Organic-rich growth checks are observed to occur directly at the end of a ridge feature (blue arrows), while not all ridge features are concluded by growth checks (purple arrow). The yellow dashed line marks boundary between inner and outer shell layers. Both Sr-labels show bright greyscales and follow the growth front of the shell. In the inner layer, the growth check continues as a prismatic**



5 layer (green arrow). Strontium-labels within the outer layer (B) show first-order prisms to consist of radially arranged second-order prisms, which in turn consist of third-order prisms with their long axis parallel to each other, as seen in a broken piece of shell (C, Fig. S11). The inner, crossed acicular layer (D, BSE image) is composed of needle-like lamellae intersecting at an angle of ca. 82°. Etched specimens (E, F: SE images) reveal the nano-granular texture of the mineral phase as well as organic compounds with fibre (red circles) and sheet-like structures (dashed red lines) in the prismatic (E) and crossed acicular (F) layers. White arrows mark the general growth direction for each ultrastructure. For more details see Fig. S5-S8. Scale bars: 100 μm (A), 5 μm (B and D), and 500 nm (C, E and F).

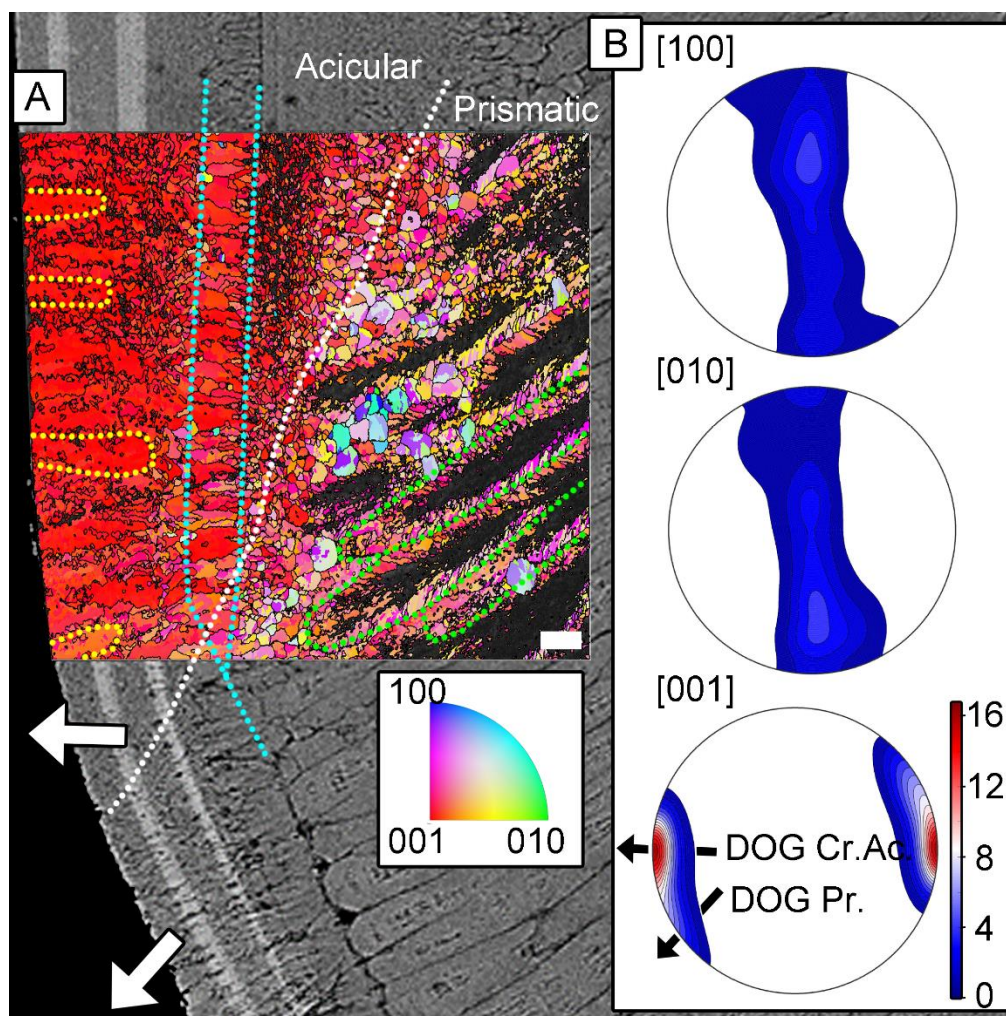
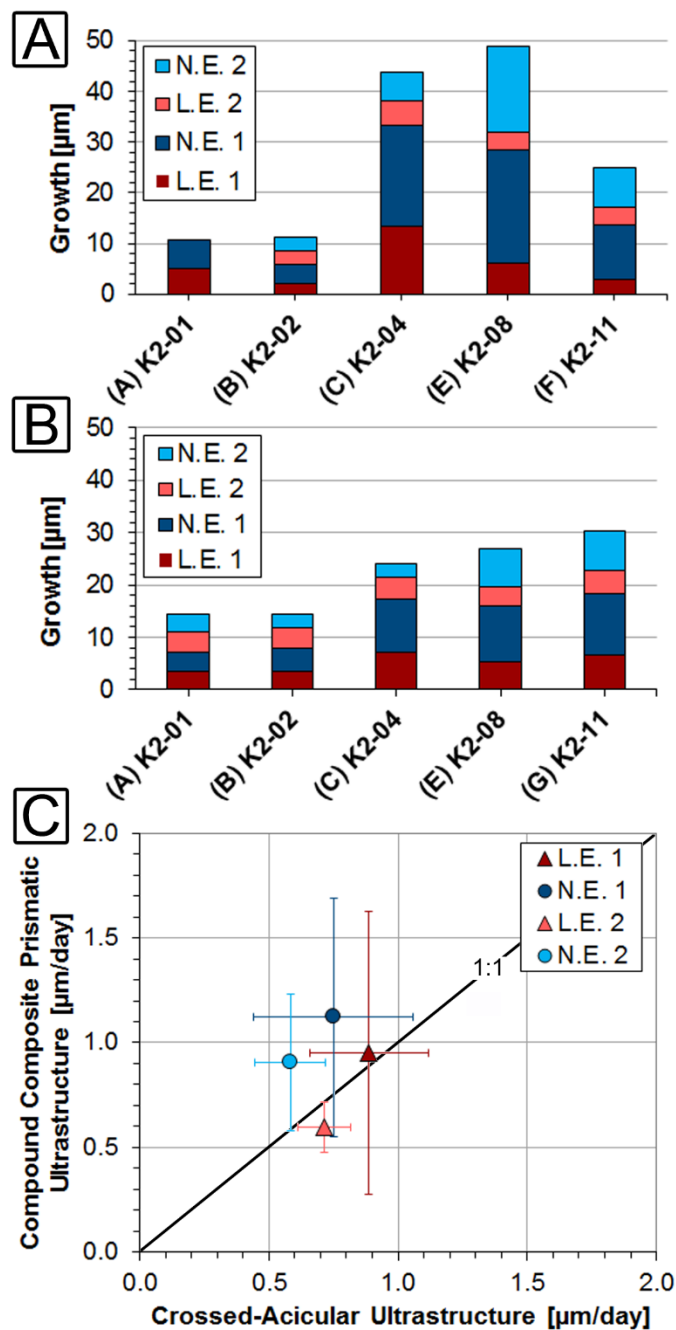
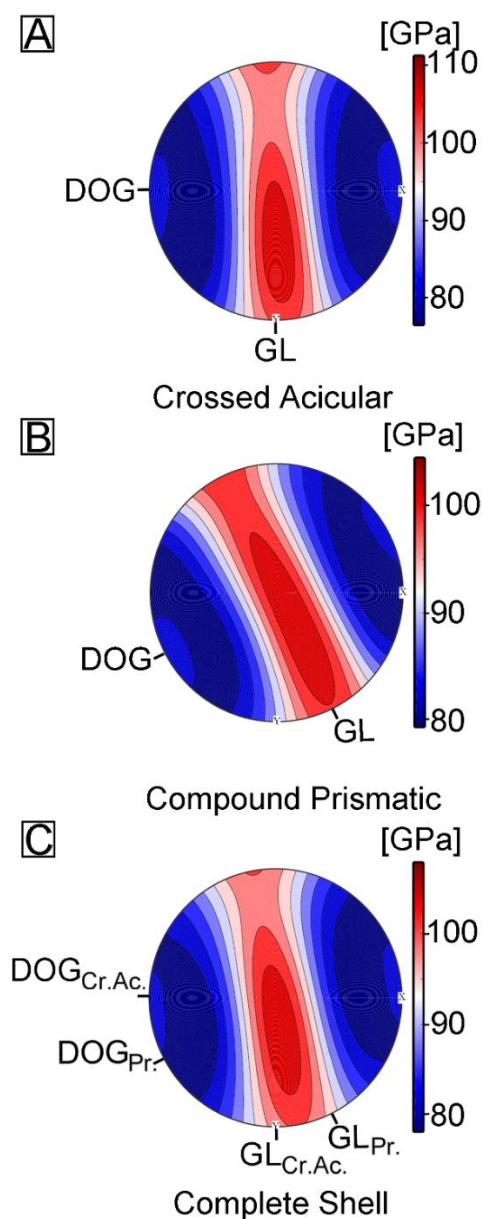


Figure 5: Orientation map for aragonite (A) of a pulsed Sr-labelled *K. rhytiphora* shell (specimen ID: K2-11). Blue, green, and red represent the crystallographic a- [100], b- [010], and c-axes [001] of aragonite, respectively. The map is color-coded to show which crystallographic axis is aligned parallel to the growth direction of the shell-layers. The dotted white line indicates the boundary between inner and outer shell layers. The organic growth check in the outer structure that transitions into a thin prismatic layer in the inner layer is highlighted with light blue dotted lines. First-order prisms in the outer structure (some green outlined) have unindexed cores, while feathery arranged second-order prisms are visible at their rims. Individual lamellae of the inner layer form co-oriented stacks up to 17 μm in size (circled yellow). Pole figures (B) (lower hemisphere, equal area projection) show a strong clustering of [001] axes for both shell layers and coincides with the growth direction of the inner layer (DOG Cr.Ac.), but is at an angle relative to the growth direction of the outer layer (DOG Pr. In B). Crystallographic a- and b-axes are randomly distributed in the plane normal to the growth direction (i.e. containing the growth lines of the inner layer). Maximum density values of pole figures are color-coded according to scale bar with the [001] axes achieving 16.79 times uniform. Scale bar is 10 μm .



5 **Figure 6:** Average growth of the outer compound composite prismatic (A) and inner crossed acicular layers (B) (Table 2). Distances were measured thrice at 5 different locations (Fig. S13, S14) along the axis of maximum growth using ImageJ. Growth rates agree well between labelling and ambient conditions and are within 1σ (C).



5 **Figure 7: Young moduli (upper hemisphere and equal area projection), for the compound composite prismatic (A) and crossed acicular structure (B) as well as complete shell (C). Calculations were made with the Hill averaging scheme and used the aragonite single crystal elastic properties of Pavese et al. (1992) and the EBSD data collected for this study as inputs (Mainprice et al., 2011). For every section, the minimum force needed to induce a fracture coexists with the local direction of growth. The shell presents a plane of greater resistance (~20-25% increase) normal to the local direction of growth and is oriented parallel to the growth lines.**



Tables:

Table 1: Geochemical composition of *K. rhytiphora* obtained from wavelength-dispersive X-ray spectrometry (WDS) electron probe micro analyser (EPMA) provided as wt.% ($\text{g}\cdot\text{g}^{-1}$) averages (Avg.) and standard deviations (Stdev.) for shell compositions grown under different conditions in the wild (“pre-aqua”), in aquaculture during labelling (“LE 1” and “LE 2”), and non-labelling (“pre-NE 1” and “NE 1”) experiments.

			Na ₂ O	MgO	SO ₃	Cl	CaO	SrO
Compound composite prismatic	Pre-Aqua	Avg.	0.72	0.03	0.10	0.04	54.38	0.12
	(n=5)	Stdev	0.06	0.02	0.04	0.01	0.20	0.03
	Pre-LE 1	Avg.	0.57	0.04	0.14	0.04	54.73	0.13
	(n=3)	Stdev	0.04	0.01	0.03	0.01	0.07	0.01
	LE 1	Avg.	0.56	0.04	0.12	0.03	52.86	2.36
	(n=3)	Stdev	0.04	0.01	0.02	0.01	0.09	0.07
Crossed Acicular*	NE 1	Avg.	0.41	0.03	0.17	0.03	54.72	0.31
	(n=3)	Stdev	0.01	0.03	0.05	0.02	0.43	0.01
	LE 2	Avg.	0.65	0.04	0.12	0.02	53.80	2.29
	(n=3)	Stdev	0.04	0.01	0.03	0.01	0.15	0.02
	Pre-Aqua	Avg.	0.75	bdl	0.05	0.02	54.01	0.11
	(n=5)	Stdev	0.09	-	0.06	0.01	0.06	0.04
	Pre-LE 1	Avg.	0.77	bdl	0.05	0.02	53.76	0.10
	(n=3)	Stdev	0.09	-	0.03	0.02	0.07	0.04
	LE 1	Avg.	0.75	bdl	0.13	0.03	53.18	1.43
	(n=3)	Stdev	0.09	-	0.07	0.01	0.06	0.04
NE 1	Avg.	0.72	0.03	0.20	0.02	54.52	0.15	
(n=3)	Stdev	0.09	0.05	0.07	0.02	0.06	0.04	
Limits of Detection:			0.05	0.02	0.04	0.01	0.04	0.02

MnO (<0.025), BaO (<0.018), P₂O₅ (<0.028), K₂O (<0.017), and FeO (<0.020), were analyzed and always below detection limits (provided in brackets as wt.%). *LE2 and NE 2 in the crossed acicular ultrastructure were too close to the edge to be measured with confidence and are excluded.



Table 2: Average growth rates from pulsed Sr-labelling experiments. Full lists of all measurements in Tables S3, S4. Rates in italics in ambient conditions NE2 were deposited within 6 days, all other rates within 12 days. Daily growth rates over the experimental period are 0.85 and 0.73 μm for the outer and inner layer, respectively, resulting in a $\sim 17\%$ higher growth rate for the outer layer.

Sample ID:	Structure:	LE 1 [$\mu\text{m}/6\text{d}$]	NE 1 [$\mu\text{m}/12\text{d}$]	LE 2 [$\mu\text{m}/6\text{d}$]	NE 2 [$\mu\text{m}/6\text{d}$] or [$\mu\text{m}/12\text{d}$]	Total growth experimental period [$\mu\text{m}/30\text{d}$] or [$\mu\text{m}/36\text{d}$]	Daily growth experimental period [$\mu\text{m}/\text{d}$]
K2-01*	Outer	5.1 \pm 0.6	5.7 \pm 0.6	n.a.	n.a.	<i>10.8 \pm 1.1</i>	0.66 \pm 0.08
	Inner	3.5 \pm 0.2	3.7 \pm 0.3	4.0 \pm 0.2	3.3 \pm 0.2	<i>14.5 \pm 0.9</i>	0.53 \pm 0.03
K2-02	Outer	2.2 \pm 0.4	3.7 \pm 0.5	2.6 \pm 0.5	2.8 \pm 0.3	<i>11.3 \pm 1.6</i>	0.39 \pm 0.08
	Inner	3.6 \pm 0.3	4.3 \pm 0.3	3.9 \pm 0.2	2.6 \pm 0.3	<i>14.4 \pm 1.1</i>	0.45 \pm 0.05
K2-04	Outer	13.3 \pm 0.9	20.0 \pm 0.6	4.8 \pm 0.7	5.8 \pm 0.8	<i>43.9 \pm 2.9</i>	1.41 \pm 0.15
	Inner	7.0 \pm 1.9	10.2 \pm 1.0	4.3 \pm 0.4	2.6 \pm 0.7	<i>24.0 \pm 3.9</i>	0.79 \pm 0.17
K2-06	Outer	3.8 \pm 1.2	10.5 \pm 1.7	3.5 \pm 0.7	12.4 \pm 1.6	30.1 \pm 1.3	0.78 \pm 0.12
	Inner	6.0 \pm 0.6	13.6 \pm 0.6	5.5 \pm 0.2	10.1 \pm 0.4	35.1 \pm 1.8	0.97 \pm 0.05
K2-08	Outer	6.4 \pm 1.8	22.3 \pm 1.6	3.5 \pm 0.9	16.9 \pm 0.5	49.2 \pm 1.2	1.23 \pm 0.13
	Inner	5.2 \pm 0.5	10.7 \pm 0.3	3.7 \pm 0.3	7.3 \pm 0.3	26.9 \pm 1.4	0.75 \pm 0.08
K2-11	Outer	2.8 \pm 0.7	10.8 \pm 1.3	3.6 \pm 0.9	7.7 \pm 1.3	24.9 \pm 4.2	0.65 \pm 0.11
	Inner	6.7 \pm 0.3	11.6 \pm 0.2	4.4 \pm 0.2	7.6 \pm 0.3	30.3 \pm 0.9	0.86 \pm 0.02
	Av. Outer	5.6 \pm 0.9	12.2 \pm 1.1	3.6 \pm 0.7	9.1 \pm 0.9	28.4 \pm 2.1	0.85 \pm 0.11
	Av. Inner	5.3 \pm 0.6	9.0 \pm 0.5	4.3 \pm 0.3	5.6 \pm 0.4	24.2 \pm 1.7	0.73 \pm 0.07

*This individual did not show prismatic growth after NE1, while the crossed acicular structure kept growing.



Table 3: Enrichment factors of Ca and Sr between shell and seawater for both ultrastructures as well as for Sr-enriched and ambient conditions. Concentrations for Ca and Sr in shell from Table 1.

Enrichment Factors:	Outer Compound Composite Prismatic Structure	Inner Crossed Acicular Structure
Labeled: $\text{Ca}_{\text{Shell/Seawater}}$	932	936
Unlabeled: $\text{Ca}_{\text{Shell/Seawater}}$	903	923
Labeled: $\text{Sr}_{\text{Shell/Seawater}}$	141	86*
Unlabeled: $\text{Sr}_{\text{Shell/Seawater}}$	142	111

*Value underestimated as analyzed area slightly exceeds label width.



References

- Addadi, L., Joester, D., Nudelman, F., and Weiner, S.: Mollusk shell formation: A source of new concepts for understanding biomineralization processes, *Chemistry—A European Journal*, 12, 980–987, 2006.
- Agbaje, O. B. A., Thomas, D. E., McInerney, B. V., Molloy, M. P., and Jacob, D. E.: Organic macromolecules in shells of *Arctica islandica*: Comparison with nacropismatic bivalve shells, *Marine Biology*, 164, 208, 2017a.
- Agbaje, O. B. A., Wirth, R., Morales, L. F. G., Shirai, K., Kosnik, M., Watanabe, T., and Jacob, D. E.: Architecture of crossed-lamellar bivalve shells: The southern giant clam (*Tridacna derasa*, Röding, 1798), *Royal Society Open Science*, 4, 170622, 2017b.
- Alia, J. M., Mera, Y. D. de, Edwards, H. G. M., Martín, P. G., and Andres, S. L.: FT-Raman and infrared spectroscopic study of aragonite-strontianite ($\text{CaSr}_{1-x}\text{CO}_3$) solid solution, *Spectrochimica Acta Part A: Molecular and Biomolecular Spectroscopy*, 53, 2347–2362, 1997.
- Allison, N., Cohen, I., Finch, A. A., and Erez, J.: Controls on Sr/Ca and Mg/Ca in scleractinian corals: The effects of Ca-ATPase and transcellular Ca channels on skeletal chemistry, *Geochimica et Cosmochimica Acta*, 75, 6350–6360, 2011.
- Almagro, I., Drzymała, P., Berent, K., Sainz-Díaz, C. I., Willinger, M. G., Bonarski, J., and Checa, A. G.: New crystallographic relationships in biogenic aragonite: The crossed-lamellar microstructures of mollusks, *Crystal Growth & Design*, 16, 2083–2093, 2016.
- Bachmann, F., Hielscher, R., Jupp, P. E., Pantleon, W., Schaeben, H., and Wegert, E.: Inferential statistics of electron backscatter diffraction data from within individual crystalline grains, *Journal of Applied Crystallography*, 43, 1338–1355, 2010.
- Bischoff, W. D., Sharma, S. K., and MacKenzie, F. T.: Carbonate ion disorder in synthetic and biogenic magnesian calcites: A Raman spectral study, *American Mineralogist*, 70, 581–589, 1985.
- Böhm, C. F., Demmert, B., Harris, J., Fey, T., Marin, F., and Wolf, S. E.: Structural commonalities and deviations in the hierarchical organization of crossed-lamellar shells: A case study on the shell of the bivalve *Glycymeris glycymeris*, *Journal of Materials Research*, 31, 536–546, 2016.
- Cann, J. H., Deckker, P. de, and Murray-Wallace, C. V.: Coastal aboriginal shell middens and their palaeoenvironmental significance, Robe Range, South Australia, *Transactions of the Royal Society of South Australia*, 115, 161–175, 1991.
- Carré, M., Bentaleb, I., Blamart, D., Ogle, N., Cardenas, F., Zevallos, S., Kalin, R. M., Ortlieb, L., and Fontugne, M.: Stable isotopes and sclerochronology of the bivalve *Mesodesma donacium*: Potential application to Peruvian paleoceanographic reconstructions, *Palaeogeography, Palaeoclimatology, Palaeoecology*, 228, 4–25, 2005.
- Carré, M., Bentaleb, I., Bruguier, O., Ordinola, E., Barrett, N. T., and Fontugne, M.: Calcification rate influence on trace element concentrations in aragonitic bivalve shells: Evidences and mechanisms, *Geochimica et Cosmochimica Acta*, 70, 4906–4920, 2006.
- Carter, J. G.: Skeletal biomineralization: patterns, processes and evolutionary trends, 1, American Geophysical Union, 1989.



- Chateigner, D., Hedegaard, C., and Wenk, H.-R.: Mollusc shell microstructures and crystallographic textures, *Journal of Structural Geology*, 22, 1723–1735, 2000.
- Checa, A. G., Cartwright, J. H. E., and Willinger, M.-G.: Mineral bridges in nacre, *Journal of Structural Biology*, 176, 330–339, 2011.
- 5 Checa, A. G., Okamoto, T., and Ramírez, J.: Organization pattern of nacre in Pteriidae (Bivalvia: Mollusca) explained by crystal competition, *Proceedings of the Royal Society of London B: Biological Sciences*, 273, 1329–1337, 2006.
- Cohen, A. L. and McConnaughey, T. A.: Geochemical perspectives on coral mineralization, *Reviews in Mineralogy and Geochemistry*, 54, 151–187, 2003.
- Currey, J. D. and Kohn, A. J.: Fracture in the crossed-lamellar structure of *Conus* shells, *Journal of Materials Science*, 11,
10 1615–1623, 1976.
- Cusack, M., Parkinson, D., Freer, A., Perez-Huerta, A., Fallick, A. E., and Curry, G. B.: Oxygen isotope composition in *Modiolus modiolus* aragonite in the context of biological and crystallographic control, *De Gruyter*, 2008.
- de Yoreo, J. J., Gilbert, P. U., Sommerdijk, N. A., Penn, R. L., Whitelam, S., Joester, D., Zhang, H., Rimer, J. D., Navrotsky, A., and Banfield, J. F.: Crystallization by particle attachment in synthetic, biogenic, and geologic environments, *Science*,
15 349, aaa6760, 2015.
- Domart-Coulon, I., Stolarski, J., Brahmi, C., Gutner-Hoch, E., Janiszewska, K., Shemesh, A., and Meibom, A.: Simultaneous extension of both basic microstructural components in scleractinian coral skeleton during night and daytime, visualized by in situ 86 Sr pulse labeling, *Journal of Structural Biology*, 185, 79–88, 2014.
- Edgar, G. J.: *Australian marine life: The plants and animals of temperate waters*, Rev. ed., Reed New Holland, Frenchs
20 Forest, N.S.W., London, 544 pp., 2000.
- Falini, G., Albeck, S., Weiner, S., and Addadi, L.: Control of aragonite or calcite polymorphism by mollusk shell macromolecules, *Science*, 271, 67–69, 1996.
- Feng, Q. L., Cui, F. Z., Pu, G., Wang, R. Z., and Li, H. D.: Crystal orientation, toughening mechanisms and a mimic of nacre, *Materials Science and Engineering: C*, 11, 19–25, 2000.
- 25 Fitzer, S. C., Zhu, W., Tanner, K. E., Phoenix, V. R., Kamenos, N. A., and Cusack, M.: Ocean acidification alters the material properties of *Mytilus edulis* shells, *Journal of The Royal Society Interface*, 12, 20141227, 2015.
- Foster, L. C., Allison, N., Finch, A. A., and Andersson, C.: Strontium distribution in the shell of the aragonite bivalve *Arctica islandica*, *Geochemistry, Geophysics, Geosystems*, 10, 2009.
- Gilbert, P., Metzler, R. A., Zhou, D., Scholl, A., Doran, A., Young, A., Kunz, M., Tamura, N., and Coppersmith, S. N.:
30 Gradual ordering in red abalone nacre, *Journal of the American Chemical Society*, 130, 17519–17527, 2008.
- Gilbert, P. U., Bergmann, K. D., Myers, C. E., Marcus, M. A., DeVol, R. T., Sun, C.-Y., Blonsky, A. Z., Tamre, E., Zhao, J., and Karan, E. A.: Nacre tablet thickness records formation temperature in modern and fossil shells, *Earth and Planetary Science Letters*, 460, 281–292, 2017.



- Gillikin, D. P., Lorrain, A., Navez, J., Taylor, J. W., André, L., Keppens, E., Baeyens, W., and Dehairs, F.: Strong biological controls on Sr/Ca ratios in aragonitic marine bivalve shells, *Geochemistry, Geophysics, Geosystems*, 6, 2005.
- Gillikin, D. P., Lorrain, A., Paulet, Y.-M., André, L., and Dehairs, F.: Synchronous barium peaks in high-resolution profiles of calcite and aragonite marine bivalve shells, *Geo-Marine Letters*, 28, 351–358, 2008.
- 5 Gorzelak, P., Stolarski, J., Dery, A., Dubois, P., Escrig, S., and Meibom, A.: Ultrascale and microscale growth dynamics of the cidaroid spine of *Phyllacanthus imperialis* revealed by 26Mg labeling and NanoSIMS isotopic imaging, *Journal of morphology*, 275, 788–796, 2014.
- Gutner-Hoch, E., Schneider, K., Stolarski, J., Domart-Coulon, I., Yam, R., Meibom, A., Shemesh, A., and Levy, O.: Evidence for Rhythmicity Pacemaker in the Calcification Process of Scleractinian Coral, *Scientific reports*, 6, 2016.
- 10 Hashin, Z.: The elastic moduli of heterogeneous materials, *Journal of Applied Mechanics*, 29, 143–150, 1962.
- Henry, H., Tilhac, R., Griffin, W. L., O'Reilly, S. Y., Satsukawa, T., Kaczmarek, M.-A., Grégoire, M., and Ceuleneer, G.: Deformation of mantle pyroxenites provides clues to geodynamic processes in subduction zones: Case study of the Cabo Ortegal Complex, Spain, *Earth and Planetary Science Letters*, 472, 174–185, 2017.
- Hovden, R., Wolf, S. E., Holtz, M. E., Marin, F., Muller, D. A., and Estroff, L. A.: Nanoscale assembly processes revealed in 15 the nacreprismatic transition zone of *Pinna nobilis* mollusc shells, *Nature communications*, 6, 10097, 2015.
- Jackson, A. P., Vincent, J. F.V., and Turner, R. M.: The mechanical design of nacre, *Proceedings of the Royal Society of London B: Biological Sciences*, 234, 415–440, 1988.
- Jacob, D. E., Soldati, A. L., Wirth, R., Huth, J., Wehrmeister, U., and Hofmeister, W.: Nanostructure, composition and mechanisms of bivalve shell growth, *Geochimica et Cosmochimica Acta*, 72, 5401–5415, 2008.
- 20 Jacob, D. E., Wirth, R., Soldati, A. L., Wehrmeister, U., and Schreiber, A.: Amorphous calcium carbonate in the shells of adult Unionoida, *Journal of Structural Biology*, 173, 241–249, 2011.
- Jones, D. S. and Quitmyer, I. R.: Marking time with bivalve shells: Oxygen isotopes and season of annual increment formation, *Palaios*, 340–346, 1996.
- Kamat, S., Su, X., Ballarini, R., and Heuer, A. H.: Structural basis for the fracture toughness of the shell of the conch 25 *Strombus gigas*, *Nature*, 405, 1036, 2000.
- Katti, K. S., Mohanty, B., and Katti, D. R.: Nanomechanical properties of nacre, *Journal of Materials Research*, 21, 1237–1242, 2006.
- Klein, R. T., Lohmann, K. C., and Thayer, C. W.: Sr/Ca and $^{13}\text{C}/^{12}\text{C}$ ratios in skeletal calcite of *Mytilus trossulus*: Covariation with metabolic rate, salinity, and carbon isotopic composition of seawater, *Geochimica et Cosmochimica Acta*, 60, 4207–4221, 1996.
- 30 Kobayashi, I. and Akai, J.: Twinned aragonite crystals found in the bivalvian crossed lamellar shell structure, *The Journal of the Geological Society of Japan*, 100, 177–180, 1994.
- Loste, E., Park, R. J., Warren, J., and Meldrum, F. C.: Precipitation of calcium carbonate in confinement, *Advanced Functional Materials*, 14, 1211–1220, 2004.



- Mainprice, D., Hielscher, R., and Schaeben, H.: Calculating anisotropic physical properties from texture data using the MTEX open-source package, Geological Society, London, Special Publications, 360, 175–192, 2011.
- Nehrke, G., Keul, N., Langer, G., Nooijer, L. J. de, Bijma, J., and Meibom, A.: A new model for biomineralization and trace-element signatures of Foraminifera tests, *Biogeosciences*, 10, 6759–6767, 2013.
- 5 Nell, J. A., O'Connor, W. A., Heasman, M. P., and Goard, L. J.: Hatchery production for the venerid clam *Katelysia rhytiphora* (Lamy) and the Sydney cockle *Anadara trapezia* (Deshayes), *Aquaculture*, 119, 149–156, 1994.
- Nell, J. A. and Paterson, K. J.: Salinity studies on the clams *Katelysia rhytiphora* (Lamy) and *Tapes dorsatus* (Lamarck), *Aquaculture Research*, 28, 115–119, 1997.
- Nudelman, F. (Ed.): *Nacre biomineralisation: A review on the mechanisms of crystal nucleation*, 46, Elsevier, 2-10, 2015.
- 10 O'Donnell, M. D., Fredholm, Y., Rouffignac, A. de, and Hill, R. G.: Structural analysis of a series of strontium-substituted apatites, *Acta Biomaterialia*, 4, 1455–1464, 2008.
- Olson, I. C., Blonsky, A. Z., Tamura, N., Kunz, M., Pokroy, B., Romao, C. P., White, M. A., and Gilbert, P. U.: Crystal nucleation and near-epitaxial growth in nacre, *Journal of Structural Biology*, 184, 454–463, 2013.
- Otter, L. M., Agbaje, O., Le Huong, T.-T., Häger, T., and Jacob, D. E.: Akoya Cultured Pearl Farming in Eastern Australia, 15 *Gems & Gemology*, 53, 2017.
- Paterson, K. J. and Nell, J. A.: Effect of different growing techniques and substrate types on the growth and survival of the clams *Tapes dorsatus* (Lamarck) and *Katelysia rhytiphora* (Lamy), *Aquaculture Research*, 28, 707–715, 1997.
- Pavese, A., Catti, M., Price, G. D., and Jackson, R. A.: Interatomic potentials for CaCO₃ polymorphs (calcite and aragonite), fitted to elastic and vibrational data, *Physics and Chemistry of Minerals*, 19, 80–87, 1992.
- 20 Pérez-Huerta, A., Cuif, J.-P., Dauphin, Y., and Cusack, M.: Crystallography of calcite in pearls, *European Journal of Mineralogy*, 26, 507–516, 2014.
- Peterson, C. H., Irlandi, E. A., and Black, R.: The crash in suspension-feeding bivalve populations (*Katelysia* spp.) in Princess Royal Harbour: An unexpected consequence of eutrophication, *Journal of Experimental Marine Biology and Ecology*, 176, 39–52, 1994.
- 25 Popov, S. V.: Composite prismatic structure in bivalve shell, *Acta Palaeontologica Polonica*, 31, 1986.
- Radermacher, P., Schöne, B. R., Gischler, E., Oschmann, W., Thébault, J., and Fiebig, J.: Sclerochronology—a highly versatile tool for mariculture and reconstruction of life history traits of the queen conch, *Strombus gigas* (Gastropoda), *Aquatic Living Resources*, 22, 307–318, 2009.
- Rhoads, D. C. and Lutz, R. A.: *Skeletal Growth of Aquatic Organisms: Biological records of environmental change*, Plenum Press, 1980.
- 30 Rodriguez-Navarro, A. B., Checa, A., Willinger, M.-G., Bolmaro, R., and Bonarski, J.: Crystallographic relationships in the crossed lamellar microstructure of the shell of the gastropod *Conus marmoreus*, *Acta Biomaterialia*, 8, 830–835, 2012.
- Ropes, J. W., Jones, D. S., Murawski, S. A., Serchuk, F. M., and Jearld, A.: Documentation of annual growth lines in ocean quahogs, *Arctica islandica* Linne, *Fish Bull*, 82, 1–19, 1984.



- Rousseau, M., Meibom, A., Gèze, M., Bourrat, X., Angellier, M., and Lopez, E.: Dynamics of sheet nacre formation in bivalves, *Journal of Structural Biology*, 165, 190–195, 2009.
- Ruschel, K., Nasdala, L., Kronz, A., Hanchar, J. M., Töbrens, D. M., Škoda, R., Finger, F., and Möller, A.: A Raman spectroscopic study on the structural disorder of monazite–(Ce), *Mineralogy and Petrology*, 105, 41–55, 2012.
- 5 Russell, M. P. and Urbaniak, L. M. (Eds.): Does calcein affect estimates of growth rates in sea urchins?, CRC Press, 53 pp., 2004.
- Sather, W. A. and McCleskey, E. W.: Permeation and selectivity in calcium channels, *Annual Review of Physiology*, 65, 133–159, 2003.
- Schindelin, J., Rueden, C. T., Hiner, M. C., and Eliceiri, K. W.: The ImageJ ecosystem: An open platform for biomedical
10 image analysis, *Molecular Reproduction and Development*, 82, 518–529, 2015.
- Schoeppler, V., Gránásky, L., Reich, E., Poulsen, N., Kloe, R. de, Cook, P., Rack, A., Pusztai, T., and Zlotnikov, I.: Biomineralization as a Paradigm of Directional Solidification: A Physical Model for Molluscan Shell Ultrastructural Morphogenesis, *Advanced Materials*, 1803855, 2018.
- Schöne, B. R., Goodwin, D. H., Flessa, K. W., and Dettman, D. L.: Sclerochronology and Growth of the Bivalve Mollusks
15 *Chione (Chionista) fluctifraga* and *C.(Chionista) cortezi*, the *Veliger*, 45, 45–54, 2002.
- Schöne, B. R., Houk, S. D., Freyre, C., Antuané D., Fiebig, J., Oschmann, W., Kröncke, I., Dreyer, W., and Gosselck, F.: Daily growth rates in shells of *Arctica islandica*: Assessing sub-seasonal environmental controls on a long-lived bivalve mollusk, *Palaios*, 20, 78–92, 2005.
- Shimamoto, M.: Shell microstructure of the Veneridae (Bivalvia) and its phylogenetic implications, 東北大學理科報告.
20 地質學, 56, 1-A40, 1986.
- Shirai, K., Sowa, K., Watanabe, T., Sano, Y., Nakamura, T., and Clode, P.: Visualization of sub-daily skeletal growth patterns in massive *Porites* corals grown in Sr-enriched seawater, *Journal of Structural Biology*, 180, 47–56, 2012.
- Simkiss, K.: The organic matrix of the oyster shell, *Comparative Biochemistry and Physiology*, 16, 427–435, 1965.
- Soldati, A. L., Jacob, D. E., Schöne, B. R., Bianchi, M. M., and Hajduk, A.: Seasonal periodicity of growth and composition
25 in valves of *Diplodon chilensis patagonicus* (d'Orbigny, 1835), *Journal of Molluscan Studies*, 75, 75–85, 2008.
- Taylor, J. D.: The shell structure and mineralogy of the Bivalvia. Introduction. *Nuculacea-Trigonacea*, *Bulletin of the British Museum (Natural History). Zoology*, 3, 1–125, 1969.
- Thébault, J., Chauvaud, L., Clavier, J., Fichez, R., and Morize, E.: Evidence of a 2-day periodicity of striae formation in the tropical scallop *Comptopallium radula* using calcein marking, *Marine Biology*, 149, 257–267, 2006.
- 30 Urey, H. C., Lowenstam, H. A., Epstein, S., and McKinney, C. R.: Measurement of paleotemperatures and temperatures of the Upper Cretaceous of England, Denmark, and the southeastern United States, *Geological Society of America Bulletin*, 62, 399–416, 1951.
- Urmos, J., Sharma, S. K., and Mackenzie, F. T.: Characterization of some biogenic carbonates with Raman spectroscopy, *American Mineralogist*, 76, 641–646, 1991.



- Vácz, T.: A new, simple approximation for the deconvolution of instrumental broadening in spectroscopic band profiles, *Applied Spectroscopy*, 68, 1274–1278, 2014.
- Villiers, J. P. R. de: *The Crystal Structures of Aragonite, Strontianite, and Witherite*, University of Illinois at Urbana-Champaign, 1967.
- 5 Wang, R. Z., Suo, Z., Evans, A. G., Yao, N., and Aksay, I. A.: Deformation mechanisms in nacre, *Journal of Materials Research*, 16, 2485–2493, 2001.
- Watson, E. B.: Surface enrichment and trace-element uptake during crystal growth, *Geochimica et Cosmochimica Acta*, 60, 5013–5020, 1996.
- Wehrmeister, U., Soldati, A. L., Jacob, D. E., Häger, T., and Hofmeister, W.: Raman spectroscopy of synthetic, geological
10 and biological vaterite: a Raman spectroscopic study, *Journal of Raman Spectroscopy*, 41, 193–201, 2010.
- Weiner, S., Addadi, L., and Wagner, H. D.: Materials design in biology, *Materials Science and Engineering: C*, 11, 1–8, 2000.
- Weiner, S. and Dove, P. M.: An overview of biomineralization processes and the problem of the vital effect, *Reviews in Mineralogy and Geochemistry*, 54, 1–29, 2003.
- 15 Weiner, S. and Traub, W.: X-ray diffraction study of the insoluble organic matrix of mollusk shells, *FEBS Letters*, 111, 311–316, 1980.
- Weiner, S., Traub, W., and Parker, S. B.: Macromolecules in mollusc shells and their functions in biomineralization [and Discussion], *Philosophical Transactions of the Royal Society of London B: Biological Sciences*, 304, 425–434, 1984.
- Wolf, S. E., Böhm, C. F., Harris, J., Demmert, B., Jacob, D. E., Mondeshki, M., Ruiz-Agudo, E., and Rodriguez-Navarro,
20 C.: Nonclassical Crystallization in vivo et in vitro (I): Process-Structure-Property relationships of nanogranular biominerals, *Journal of Structural Biology*, 2016.
- Wolf, S. E., Lieberwirth, I., Natalio, F., Bardeau, J.-F., Delorme, N., Emmerling, F., Barrea, R., Kappl, M., and Marin, F.:
25 Merging models of biomineralisation with concepts of nonclassical crystallisation: Is a liquid amorphous precursor involved in the formation of the prismatic layer of the Mediterranean Fan Mussel *Pinna nobilis*?, *Faraday Discussions*, 159, 433–448, 2012.
- Younis, S., Kauffmann, Y., Bloch, L., and Zolotoyabko, E.: Inhomogeneity of nacre lamellae on the nanometer length scale, *Crystal Growth & Design*, 12, 4574–4579, 2012.
- Zhang, G. and Xu, J.: From colloidal nanoparticles to a single crystal: New insights into the formation of nacre's aragonite
30 tablets, *Journal of Structural Biology*, 182, 36–43, 2013.